

Effect of Synthetic Jets Actuator Parameters on Deep Reinforcement Learning-Based Flow Control Performance in a Square Cylinder

Wang Jia (贾旺)¹ and Hang Xu (徐航)¹

State Key Lab of Ocean Engineering, School of Naval Architecture, Ocean and Civil Engineering, Shanghai Jiao Tong University, Shanghai, 200240, China

(*Electronic mail: hangxu@sjtu.edu.cn)

(Dated: 24 May 2024)

We utilize deep reinforcement learning (DRL) algorithms to precisely control the mass flow rates of synthetic jets located on the upper and lower surfaces of a square cylinder for active flow control. Through DRL-based active flow control (AFC) technology, we significantly reduce the lift and drag coefficients of the square cylinder at Reynolds number (Re) = 100 and Re = 500, while completely suppressing vortex shedding in the wake flow field. Additionally, we conduct a sensitivity analysis of the position and width parameters of the synthetic jets regarding flow control performance. Our observations indicate that positioning the synthetic jets near the trailing edge corners of the square cylinder, rather than the leading edge corners, can completely suppress vortex shedding, resulting in more stable lift and drag coefficients in the controlled flow. When the synthetic jets are positioned at the trailing edge corners, flow control reduces the mean drag coefficient by 14.4% and the standard deviation of the lift coefficient by 86.1% for the baseline flow at Re = 100. For the baseline flow at Re = 500, flow control reduces the mean drag coefficient by 51.4% and the standard deviation of the lift coefficient by 90.5%. At both Reynolds numbers, vortex shedding in the wake flow field is completely suppressed. Furthermore, using narrower synthetic jets results in a lower reduction rate of the standard deviations of the lift and drag coefficients, while increasing the mean and standard deviation of the mass flow rate of the jets used for flow control. This study provides guidance on optimizing the width and position of synthetic jets for DRL-based active flow control.

I. INTRODUCTION

In the backdrop of advancements in sophisticated algorithms, computational hardware, open-source software and the integration of vast amounts of data in the era of big data, scientific inquiry is transitioning from first principles to data-driven methods.¹ The field of fluid dynamics is also benefiting from this trend, with machine learning offering sophisticated algorithms capable of handling high-dimensional, large-scale fluid dynamics data, establishing mathematical modeling frameworks, and providing integrated, modular packages and libraries as open-source resources. Machine learning excels in tasks like feature extraction, modal analysis, and data mining, providing techniques for extracting insights from datasets.² Experimental fluid dynamics measurements and numerical simulation generate extensive datasets, making them ideal candidates for techniques capable of handling high-dimensional, large-scale data.³ Furthermore, machine learning algorithms can embed physical information from the field of fluid dynamics and adaptively perform tasks related to execution, control, and optimization.^{4,5} The field of flow control is rapidly advancing, propelled by the development of state-of-the-art machine learning algorithms and unprecedented volumes of data from high-precision numerical simulations across multiple spatiotemporal scales.^{1,3-5}

Active Flow Control (AFC) is an advanced fluid management strategy aimed at enhancing fluid properties and performance through proactive interventions in the flow field. By introducing energy or momentum, AFC alters the fluid's natural state, employing techniques such as fluid injection and suction, synthetic jets, and electromagnetic control.^{6,7} Synthetic jet technology produces jets by cyclically inhaling and expelling fluid from a fixed location, requiring no external energy source.⁸ This method offers several advantages, including independence from external fluid sources, high controllability, low energy consumption, and suitability for operation in narrow or complex spaces.^{9,10} These advantages render synthetic jets particularly promising tools for present and future flow control technologies.^{11,12} AFC is widely applied across various sectors, including aerospace, automotive, energy production, and environmental engineering, where it serves to reduce drag, control vortices, enhance lift, and stabilize flows.^{13,14} Despite its considerable advantages, the implementation and practical application of AFC face challenges due to the system's strong nonlinearity, high dimensionality, and time delays. Recent advancements in machine learning algorithms and control theory are propelling progress in adaptive, real-time intelligent control, facilitating more effective management of complex flow dynamics and further augmenting the capabilities of AFC technologies.¹⁵⁻¹⁷

Deep Reinforcement Learning (DRL) merges the capabilities of Deep Learning (DL) for processing high-dimensional data with the decision-making and policy optimization strengths of Reinforcement Learning (RL).^{18,19} DRL is recognized for its ability to learn and adapt autonomously, enabling end-to-end learning that is highly applicable across complex environments. DRL has demonstrated exceptional performance in a wide range of domains, including game AI, robotic control, autonomous driving, resource management and scheduling, and financial trading. It is capable of autonomously learning optimal decision-making strategies in complex environments, surpassing human-level capabilities.²⁰⁻²² DRL is a sophisticated blend of DL and RL, two powerful branches of machine learning. It combines the feature extraction capabilities of DL for complex high-dimensional data

with the decision-making abilities of RL through interactions with the environment.^{23,24} This synergy allows DRL to excel in environments that require both advanced perception and precise control. Despite challenges related to sample efficiency and stability, DRL demonstrates remarkable potential on a variety of challenging decision-making problems.^{24,25}

Given the significant potential of DRL in control and optimization, a large number of scholars have been applying it in the field of flow control. Rabault *et al.*²⁶ pioneered the application of DRL to AFC technologies, achieving an 8% reduction in drag around a cylinder at $Re = 100$. This seminal work sparked interest in applying DRL techniques within the field of fluid dynamics. Tang *et al.*²⁷ focused on the robustness across different Reynolds numbers, while Paris, Beneddine, and Dandois²⁸ explored the impact of probe distribution on control performance. Li and Zhang²⁹ applied DRL-based AFC to cylinders under various blockage ratios, integrating flow physics mechanisms during the control process to achieve significant outcomes. Fan *et al.*³⁰ developed an active flow control strategy based on DRL through experimental fluid dynamics, demonstrating the effectiveness of applying reinforcement learning in experimental fluid mechanics. Rabault and Kuhnle³¹ and Jia and Xu³² addressed issues related to parallel strategies and training when coupling Computational Fluid Dynamics (CFD) codes with DRL framework in parallel computing environments. Wang *et al.*³³ developed an open source library that integrated CFD code OpenFoam with DRL framework TensorForce. DRL has demonstrated excellent control performance in the field of AFC, sparking increasing exploration. There has been applications from low to relatively high Reynolds numbers, transitions from 2D to 3D configurations, shifts from numerical simulations to fluid experiments, and geometric changes in the body of interest from circular to square bodies. While there is a plethora of related work, we will not delve into each individually. Instead, we summarize in Table. I some relevant research on the application of DRL-based AFC methods in the context of flow around bluff bodies.

TABLE I: Summary of studies on AFC strategies for various bluff bodies.

Re	Bluff Body	Reference	Strategy	Control Algorithm	Solver	Drag Reduction	Vortex Suppressed
100	Cylinder	Rabault <i>et al.</i> ²⁶	Synthetic Jets	PPO	FeniCS	8%	-
100	Cylinder	Wang <i>et al.</i> ³³	Synthetic Jets	PPO	OpenFOAM	8%	-
100	Cylinder	Castellanos <i>et al.</i> ³⁴	Synthetic Jets	LGPC/PPO	FeniCS	8%	-
100	Cylinder	Jia and Xu ³⁵	Synthetic Jets	PPO	OpenFOAM	8%	YES
100	Cylinder	Ren, Wang, and Tang ³⁶	WSLB	PPO	LBM	-	-
120	Cylinder	Paris, Beneddine, and Dandois ²⁸	Synthetic Jets	S-PPO-CMA	FastS	18.4%	-
≤ 200	Cylinder	Li and Zhang ²⁹	Synthetic Jets	PPO	Nek5000	-	YES
100-300	Cylinder	He <i>et al.</i> ³⁷	Synthetic Jets	PPO	OpenFOAM	6%-24%	-
100-400	Cylinder	Tang <i>et al.</i> ³⁸	Synthetic Jets	PPO	FeniCS	6%-39%	-
1,000	Cylinder	Ren, Rabault, and Tang ³⁹	Synthetic Jets	PPO	LBM	30%	-
10,160	Cylinder	Fan <i>et al.</i> ³⁰	Cylinders	TD3	Lilypad	30%	-
100	Ellipse	Jia and Xu ³⁵	Synthetic Jets	PPO	OpenFOAM	16%	YES
100	Square	Wang <i>et al.</i> ³³	Synthetic Jets	SAC	OpenFOAM	14%	-
100	Square	Chen <i>et al.</i> ⁴⁰	Synthetic Jets	SAC	OpenFOAM	14%	YES
100	Square	Xia <i>et al.</i> ⁴¹	Synthetic Jets	SAC and TQC	FEniCS	17.3%	-
100-400	Square	Jia and Xu ⁴²	Synthetic Jets	SAC	OpenFOAM	14%-47%	YES
500-2,000	Square	Yan <i>et al.</i> ⁴³	Synthetic Jets	SAC	OpenFOAM	44%-61%	-

The research in the above table demonstrate the wide range of applications of DRL in the field of active flow control. These research significantly extend beyond the initial study of flow past a cylinder at $Re = 100$ by Rabault *et al.*²⁶. However, the effectiveness of DRL control algorithm varies across different work. This is especially evident among the body of research on square cylinders. As the sharp corners and straight edges force the fluid to separate at the leading edge, flows around square cylinders are characterized by complex wake structures and shedding vortices.⁴⁴⁻⁴⁶ The highly nonlinear and unique flow features makes it extremely challenging to determine the optimal control strategy. Hence, many different control experiments have been devised heuristically, leading to varying degrees of control effectiveness.

Wang *et al.*³³ initially applied the Soft Actor-Critic (SAC) algorithm to active flow control of a square cylinder, achieving a 13.7% reduction in drag at $Re = 100$. Despite this significant reduction, vortex shedding behind the cylinder is still evident. Xia *et al.*⁴¹ conduct active flow control around a square cylinder at $Re = 100$ using RL, training with an augmented state that includes both current and past measurements and actions, which are represented by a nonlinear auto-regressive exogenous model to address issues of partial observability. Jia and Xu⁴² employed the SAC algorithm to regulate the flow from synthetic jets positioned on the upper and lower surfaces of a constrained square cylinder at $Re = 100, 200, 300,$ and 400 . The research results demonstrated that the active control strategy based on the SAC algorithm effectively reduces drag by approximately 14.4%, 26.4%, 38.9%, and 47.0% respectively. A distinctive feature of this study compared to others is its success in suppressing vortex shedding behind the square cylinder across the range of Reynolds numbers from 100 to 400. This DRL-based AFC delivers an energy-efficient control strategy that not only reduces drag and suppresses lift but also effectively suppresses vortex shedding.

Yan *et al.*⁴⁷ investigated the impact of multiple jet actuators on drag and lift reduction for rectangular cylinders with four different aspect ratios at $Re = 1,000$, employing DRL for control. Specifically, the deployment of four synthetic jets resulted in an average drag reduction of 63.2%, while eight jets achieved a 77.1% reduction. This study investigated various jet distribution strategies, emphasizing the importance of multi-jet actuation in enhancing aerodynamic performance.

Additionally, an intriguing research question that captures the interest of many scholars is the optimal placement of synthetic jets for control effectiveness. Particularly noteworthy are two studies that have arrived at markedly different conclusions, prompting further reflection and analysis within the research community.^{40,43} Chen *et al.*⁴⁰ employ DRL-based AFC to mitigate vibrations induced by lift on a square cylinder at $Re = 100$. Their study investigates the effect of jets positioning on control efficacy, examining positions near the leading edge, midpoints of the sidewalls, and near the trailing edge of the cylinder. Results indicate that for reducing lift-induced vibrations and drag coefficient, positioning the jets near the trailing edge is significantly superior to placement near the leading edge or midpoints of the sidewalls. Moreover, complete suppression of vortex shedding behind the square cylinder occurs only when the jets are placed near the trailing edge. Yan *et al.*⁴³ examined the impact of symmetrically deploying jet actuators at both the front and trailing corners of a square cylinder under flow configurations at $Re = 500, 1,000$ and $2,000$. The findings reveal that positioning jets near the front corners provides more effective control over lift and drag coefficients compared to placement near the trailing corners. Despite these modifications, vortex shedding in the controlled flow was not suppressed at any of the three Reynolds numbers.

Given the current state of the art in DRL-based AFC of flow around square cylinders, it is evident that there is a lack of parameterization for synthetic jets to reconcile the varying degrees of control effectiveness in literature. Consequently, our research is motivated by two main reasons. Firstly, there is currently no study that has successfully used AFC to achieve both efficient drag reduction and complete suppression of vortex shedding at Reynolds numbers greater than 500. Secondly, previous studies have shown that the effects of synthetic jets placement on control performance exhibit different outcomes at $Re = 100$ and $Re = 500$. We are interested in exploring whether it is possible, at $Re = 100$ and $Re = 500$, to use AFC based on DRL to achieve both efficient drag reduction and complete suppression of vortex shedding. Additionally, we design two synthetic jet placements and four synthetic jet widths to conduct a thorough analysis of their impacts on flow control performance. The parameterized design of control experiments and corresponding analysis aim to provide valuable references for the control of flow around square cylinders. The structure of this paper is as follows. In Sec. II, we introduce the DRL framework, which consists of a fluid simulation environment and the SAC agent. In Sec. III, we present and discuss the results. Initially, we describe the Baseline and the Base flow. Then, we discuss the convergence performance of DRL at $Re = 100$ and $Re = 500$. Finally, we analyze the effects of the placement and width of synthetic jets on control performance. In Sec. IV, we summarize the main conclusions of this study and discuss the broader implications of these findings.

II. PROBLEM DESCRIPTION AND METHODOLOGY

We develop a DRL framework that enables interaction between the agent and the numerical simulation environment, validated in flow regimes characterized by two-dimensional vortex shedding. In our DRL framework, the agent observes the current state of the CFD environment and interacts with it to adjust the mass flow rates of two synthetic jets on the square cylinder, based on feedback from reward signals. Through an iterative optimization process, the SAC agent gradually approaches the optimal flow control strategy by learning and trial-and-error, thereby achieving multiple control objectives such as reducing lift and drag coefficients and suppressing vortex shedding. The specific operational process is depicted in Fig. 1. Sec. II A provides detailed information about the flow environment. Sec. II B elaborates on the ML techniques discussed in this paper, including reinforcement learning, deep learning, and deep reinforcement learning. Sec. II C introduces the key components for performing active flow control using DRL methods, as well as the software and hardware configurations relevant to training.

A. Flow environment

In the present study, we analyze the flow past a two-dimensional square cylinder, as illustrated in Fig. 2. To construct the physical model, we establish a Cartesian coordinate system with the center of the square cylinder as the origin. The flow direction is defined as the positive x -axis, while the direction perpendicular to the flow is designated as the positive y -axis. The square cylinder has a side length denoted by D . The computational domain extends $30D$ downstream from the center of the square cylinder to define the outlet boundary, and $10D$ upstream to establish the inlet. The lateral boundaries extend $10D$ from the center of the square cylinder on both the left and right sides. This configuration results in a rectangular computational domain with dimensions of $40D$ in the streamwise direction and $20D$ in the spanwise direction.

To comprehensively explore the impact of synthetic jets arrangement on control performance, we address two key aspects: the placement and width of the synthetic jets. Given that the flow separation points around the square cylinder are fixed, occurring at the leading and trailing edge corners, we strategically position the synthetic jets at these corner points in our study. Specifically, placement variations include positions near both the leading and trailing edges of the square cylinder. Furthermore,

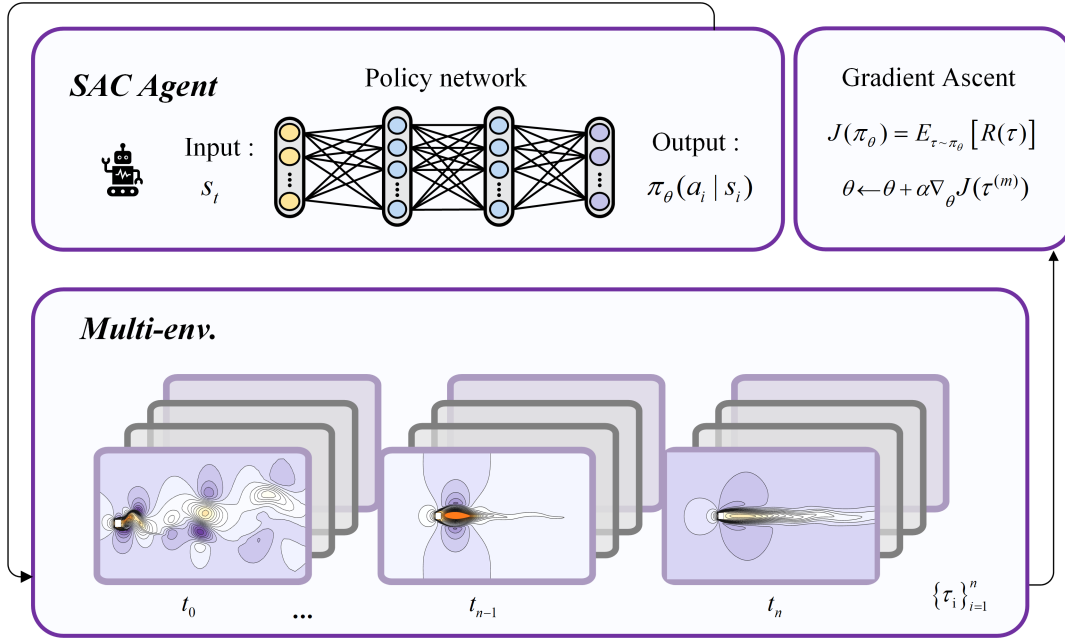


FIG. 1: A multi-environment parallel DRL training framework, in which the agent adopts the SAC type and the environment is set to numerical simulation environment. The parallel computation across n environments yields a set of trajectories $\{\tau_i\}_{i=1}^n$, with each trajectory τ_i comprising the sequence of states, actions, and rewards as $\tau_i = \{(s_0, a_0), (s_1, a_1, r_1), \dots, (s_T, a_T, r_T)\}$, where (s_t, a_t, r_t) represents the state, action, and reward at time-step t , respectively, for the i -th environment. The parameters θ of the policy network are updated using gradient ascent, i.e., $\theta \leftarrow \theta + \alpha \nabla_\theta J(\pi_\theta)$, where α denotes the learning rate.

the widths of the synthetic jets are designed to encompass $D/20, D/25, D/30$, and $D/35$, where D represents the side length of the square cylinder. By systematically varying these parameters, we aim to provide a detailed analysis of their effects on flow control performance. The synthetic jets on the upper and lower walls of the square cylinder are set up with a uniform velocity distribution, where the magnitude of the jet velocity represents non-dimensional mass flow rates, and the direction of the jet velocity is along the outward normal vector. The total mass flow rate of the two jets is zero, which more accurately reflects real-world applications compared to adding or removing mass from the system. This ensures that any observed drag reduction can be attributed to the effectiveness of the flow control strategy, rather than to any propulsive effect. Fig. 2 illustrates the schematic placement of the synthetic jets on the square cylinder, positioned near the leading or trailing edge corners.

The Navier-Stokes equations for an incompressible viscous fluid in a domain $\Omega \subset \mathbb{R}^{nd}$ over a time interval $(0, T)$ are fundamental in fluid dynamics. These equations describe how the velocity field $\mathbf{u} = \mathbf{u}(\mathbf{x}, t)$ and pressure field $p = p(\mathbf{x}, t)$ of the fluid evolve over time, where \mathbf{x} represents the spatial coordinates and t represents time.

$$\frac{\partial \mathbf{u}}{\partial t} + \mathbf{u} \cdot (\nabla \mathbf{u}) = -\nabla p + Re^{-1} \Delta \mathbf{u} \quad \text{on } \Omega \times (0, T), \quad (1a)$$

$$\nabla \cdot \mathbf{u} = 0 \quad \text{on } \Omega \times (0, T). \quad (1b)$$

Here, $Re = \frac{\bar{U}D}{\nu}$ is the Reynolds number, where \bar{U} is the mean velocity at the inlet and ν is the kinematic viscosity. Together, these equations articulate the fundamental behaviors of fluid flow, linking the dynamics of velocity changes to the principle of mass conservation in fluid mechanics.

In the simulation setup described, the inlet of the computational domain is characterized by a uniform velocity distribution. Specifically, the velocity at the inlet is set to a magnitude of 2, with the direction aligned along the x -axis. The outlet of the computational domain adopts *Neumann-type* boundary conditions to ensure that the stress vector is zero to simulate the natural flow behavior at infinite distance. The upper and lower boundaries of the domain are designated as far-field boundary conditions, aimed at minimizing their impact on the flow around the square cylinder and approximating an unbounded fluid domain as closely as possible. The synthetic jets are configured such that their velocity direction is perpendicular to the walls of the square cylinder, directed along the outward normal of the walls. Except for the locations of the synthetic jets, all other parts of the square cylinder's walls are treated with no-slip solid wall boundary conditions, ensuring that the fluid does not penetrate

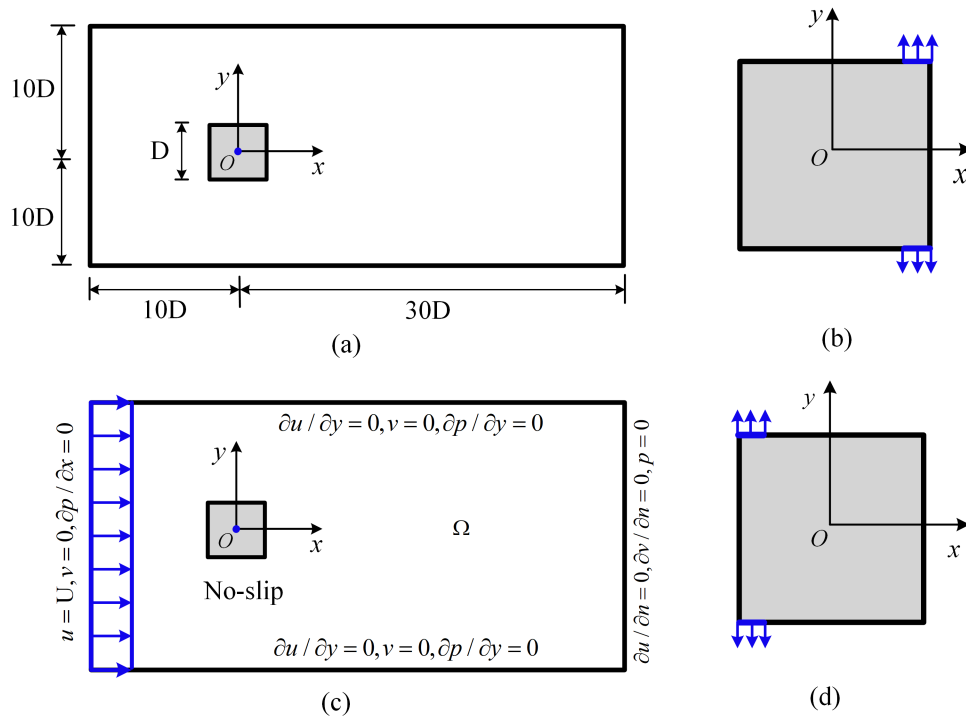


FIG. 2: A schematic of the computational domain and boundary conditions. (a) Establishment of the coordinate system and detailed dimensions of the computational domain. Note that while the dimensions of the square cylinder and computational domain are accurately labeled, the relative proportions are not to scale and are intended for illustrative purposes only. (b) Placement of the synthetic jets near the trailing corner point. (c) Specification of the boundary conditions for the computational domain. (d) Location of the synthetic jets near the leading corner points.

these surfaces and accurately reflecting the physical constraints imposed by solid boundaries on fluid flow. In addition, The boundary conditions are marked in detail in Fig. 2.

Fig. 3 illustrates the discretization of the computational domain into 23,264 quadrilateral mesh elements via a structured grid approach. Fig. 3(a) provides a detailed depiction of the discretization across the entire computational domain, with finer mesh scales near the square cylinder and coarser mesh scales near the boundary walls. Fig. 3(b) exclusively demonstrates the transition of mesh scale from coarse to fine. Fig. 3(c) demonstrates the refinement of the mesh surrounding the square cylinder, where the quadrilateral mesh elements are approximately square, ensuring accurate capture of flow field structures in fluid dynamics calculations.

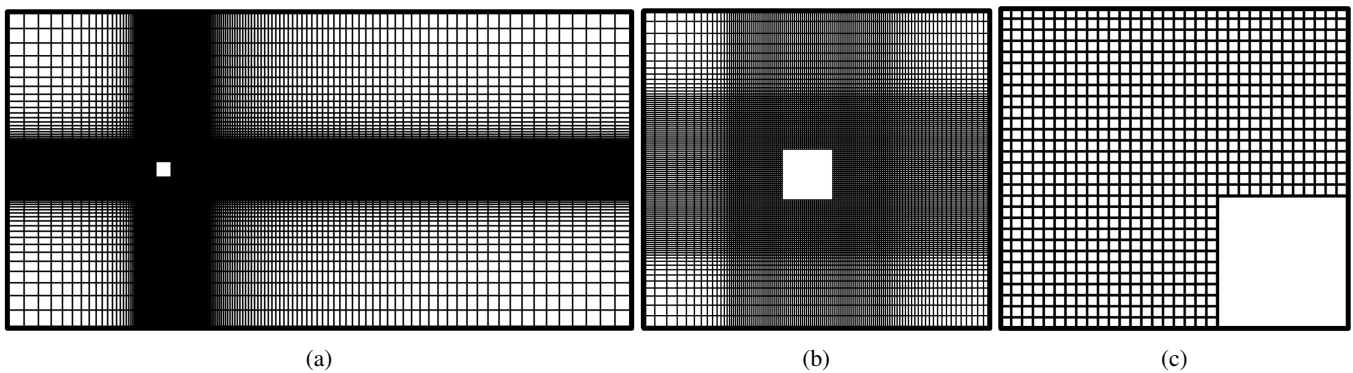


FIG. 3: Computational domain discretization. (a) Discretization scheme covering the entire computational domain. (b) Magnified depiction of the grid structure close to the square cylinder. (c) Meshing of a quarter of the square cylinder.

The bluff body drag coefficient (C_D) and lift coefficient (C_L) are defined as

$$C_D = \frac{F_D}{\frac{1}{2}\rho_\infty U_\infty^2 D}, \quad C_L = \frac{F_L}{\frac{1}{2}\rho_\infty U_\infty^2 D}. \quad (2)$$

Where F_D and F_L are the drag and lift forces, defined as the surface integrals of the pressure and viscous forces on the bluff body with respect to the x -axis and y -axis, respectively. ρ_∞ denotes the density of the fluid far from the square cylinder. U_∞ , the freestream velocity of the fluid, represents the undisturbed velocity far from any obstacles or boundaries, and it is equal to 2.

The Strouhal number (St) is used to describe the characteristic frequency of oscillatory flow phenomena and is defined as follows:

$$St = \frac{f_s \cdot D}{U_\infty}. \quad (3)$$

Where f_s is the shedding frequency calculated based on the periodic evolution of the C_L and $U_\infty = 2$.

In the current study, the incompressible flow dynamics are analyzed using the open-source CFD toolkit, OpenFOAM, as outlined by Jasak *et al.*^{48,49}. OpenFOAM stands as a rigorously tested and extensively applied computational framework that offers a comprehensive suite of numerical algorithms for the resolution of the Navier-Stokes equations. The solver implemented within OpenFOAM employs the finite volume method for the discretization of the computational domain, subdividing it into a structured mesh of control volumes. The numerical simulations were conducted using the `pimpleFoam` solver to solve the unsteady Navier-Stokes equations. The temporal discretization employed the `Backward` scheme, while the divergence discretization of the velocity field was implemented using the `Gauss linear` scheme, and the gradient discretization of the velocity utilized the `leastSquares` method. These discretization schemes were selected to ensure the requisite mathematical precision and stability for the simulation of fluid flow dynamics. To promote numerical stability within the simulations, the time step size is meticulously selected as $\Delta t = 0.0005$.

To verify the accuracy of the grid, this study conducted a grid convergence investigation. We compared results from three different grid scales and contrasted them with computational outcomes from other studies, summarizing the findings in Table. II. The table lists the values for the mean drag coefficient ($C_{D,Mean}$), the standard deviation of the drag coefficient ($C_{D,Std}$), the standard deviation of the lift coefficient ($C_{L,Std}$), and the St at $Re = 100$ and $Re = 500$. All three grids utilized structured meshes, differing only in the level of refinement, with the number of grid cells detailed in the table. The computational results in Table. II demonstrate that the differences among the three grid resolutions are insignificant and consistent with values obtained in existing literature. In the subsequent advanced DRL training phase, the main grid scheme is employed to balance computational accuracy and cost-effectiveness, ensuring the required precision is achieved while minimizing computational overhead.

TABLE II: Grid independence test for a square cylinder.

Configuration	Case	Cell number	$C_{D,Mean}$	$C_{D,Std}$	$C_{L,Std}$	St
$Re = 100$	Coarse	16,400	1.471	2.023	0.196	0.148
	Main	23,264	1.548	1.924	0.171	0.145
	Fine	28,450	1.533	1.910	0.173	0.145
	Sen, Mittal, and Biswas ⁴⁶	-	1.53	-	-	0.145
	Sharma and Eswaran ⁵⁰	-	1.49	-	-	0.150
	Singh <i>et al.</i> ⁵¹	-	1.51	-	-	0.147
$Re = 500$	Coarse	16,400	2.070	0.481	0.036	1.130
	Main	23,264	2.064	0.448	-0.042	0.127
	Fine	28,450	2.067	0.419	-0.001	0.128
	Cao, Ge, and Tamura ⁵²	-	2.050	-	-	0.133
	Bai and Alam ⁵³	-	1.940	-	-	0.136
	Sohankar, Norberg, and Davidson ⁵⁴	-	1.870	-	-	0.126

B. Machine learning

In machine learning, three main paradigms exist: supervised learning, unsupervised learning, and reinforcement learning. Supervised learning uses labeled examples to predict labels for unlabeled inputs. Unsupervised learning discovers patterns in unlabeled data. Reinforcement learning involves interacting with an environment to maximize cumulative rewards.

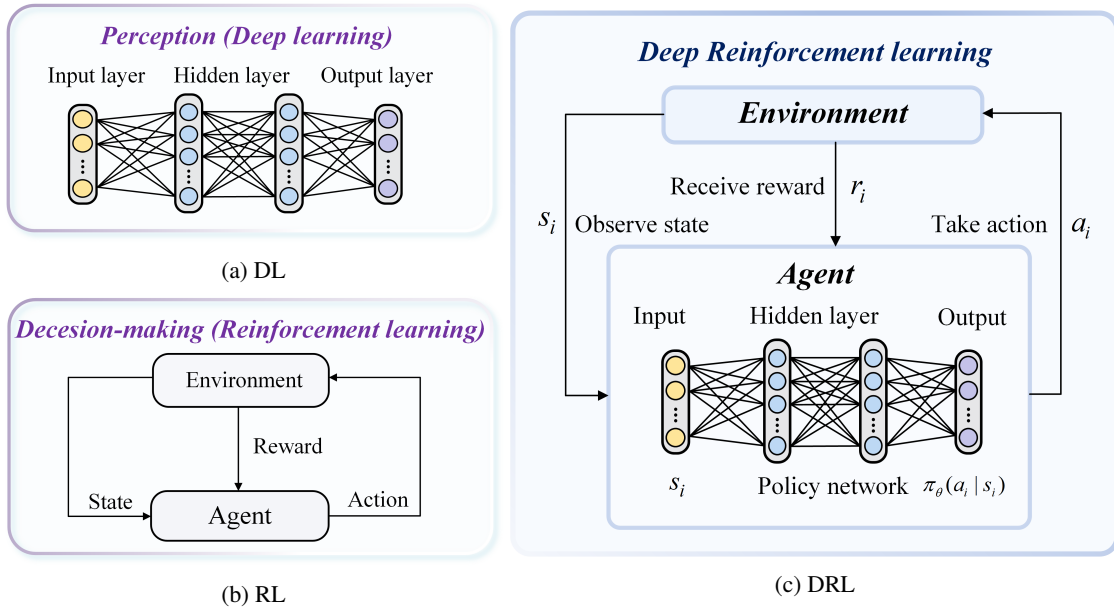


FIG. 4: Basic architectures of DL, RL, and DRL. (a) DL; (b) RL; (c) DRL.

a. Deep learning DL, a subfield of machine learning, focuses on artificial neural networks inspired by biological neural networks. These networks, depicted in Fig. 4(a), comprise interconnected layers of nodes or neurons. Each layer performs specific transformations on its inputs before passing them to the next layer. The term 'depth' in deep learning refers to the multiple layers of the neural network, comprising numerous linear and nonlinear processing units. Multiple layers enable these networks to perform complex transformations at various levels of abstraction, enhancing their ability to model intricate relationships in data. DNNs typically utilize backpropagation for training, adjusting neuron weights based on error rates from previous epochs. This process, combined with advanced optimization algorithms like Adam or stochastic gradient descent, efficiently minimizes the loss function.

b. Reinforcement learning RL is a crucial branch of machine learning that focuses on the interaction between an agent and its environment. As illustrated in Fig. 4(b), the environment is the entity with which the agent interacts. RL aims to maximize cumulative rewards by learning optimal behavior or policies through trial and error during these interactions. A finite Markov Decision Process (MDP) is defined by the tuple (S, A, P, R, γ) , where S is the finite state space, A is the finite action space, P is the state transition probability function, and R is the reward function. γ is the discount factor, representing the importance given to future rewards relative to immediate rewards. At each time-step i , the agent observes the environment in state s_i , selects an action a_i , resulting in a transition to state s_{i+1} with a probability $p(s_{i+1}|s_i, a_i)$. The agent receives a reward R associated with this transition. The agent's decision-making process is governed by a policy denoted as $\pi(a_i|s_i)$.

c. Deep Reinforcement learning As shown in Fig. 4(c), embedding DNNs into the basic RL framework constitutes the most fundamental DRL structure. DRL integrates DL with RL to manage complex decision-making tasks in high-dimensional environments. Within this integration, DL plays a pivotal role in estimating several key functions critical to the RL process. DRL utilizes DNNs as function approximators to model complex value functions and policy functions, which are otherwise challenging to address with conventional RL methods. The state value function ($V_\pi(s)$) estimates the expected cumulative reward that can be obtained from a particular state s under a given policy π . The formula for $V_\pi(s)$ is expressed as:

$$V_\pi(s) = \mathbb{E}_\pi \left[\sum_{t=0}^{\infty} \gamma^t R_t \mid s_t = s \right], \quad (4)$$

where \mathbb{E}_π denotes the expectation under policy π , γ is the discount factor, R_t represents the reward at time step t , and s_t denotes the state at time step t . DNNs approximate $V_\pi(s)$, enabling the handling of large and complex state spaces. The action-value function ($Q_\pi(s, a)$) estimates the expected cumulative reward from taking action a_t in state s_t and subsequently following policy π . The formula for $Q_\pi(s, a)$ is expressed as:

$$Q_\pi(s, a) = \mathbb{E}_\pi \left[\sum_{t=0}^{\infty} \gamma^t R_t \mid s_t = s, a_t = a \right], \quad (5)$$

where a_i denotes the action at time step t . The remaining symbols keep the same meaning as in $V_\pi(s)$. DNNs are employed to approximate $Q_\pi(s, a)$, facilitating the evaluation of action values in extensive action spaces. Also, DNNs are commonly used as function approximators to model policy functions. The policy $\pi(a_i|s_i)$ is represented by a neural network, which outputs the probabilities of selecting each possible action given a state. Additionally, the transition function $P(s_{i+1} | s_i, a_i)$ predicts the next state s_{i+1} given the current state s_i and action a_i . DNNs can approximate this function to help the agent simulate and plan future actions more effectively.

d. Soft Actor-Critic Algorithm The SAC algorithm is a state-of-the-art deep reinforcement learning method that combines Actor-Critic techniques with off-policy learning. SAC is highly efficient, stable, and robust, particularly for tasks with continuous action spaces. Its performance relies on experience replay, Actor-Critic architecture, and entropy regularization, which together foster accelerated learning and balanced policy exploration. The data collection and network parameter update process of the SAC algorithm is illustrated in Fig. 5. The agent interacts with the environment, selecting actions according to its current

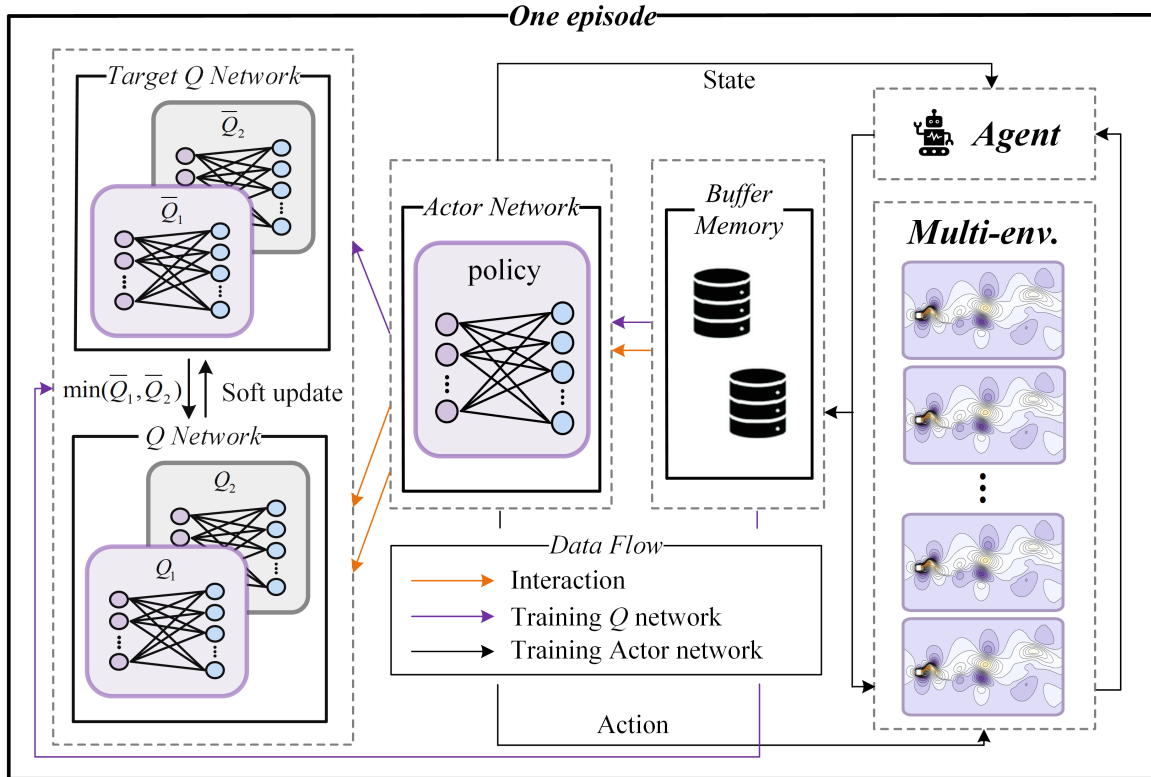


FIG. 5: The SAC algorithm collects experience data through interaction with the environment, storing it in a replay buffer. It updates the value network, policy network, and target value network, using entropy regularization to encourage exploration, resulting in an efficient and stable reinforcement learning policy.

policy π . The experience tuples (s_i, a_i, r_i, s_{i+1}) collected from these interactions are stored in a replay buffer. When updating the network parameters, the algorithm samples batches of experience data from the replay buffer. Moreover, entropy (\mathcal{H}) is a metric that quantifies the uncertainty of a random variable. Within the framework of reinforcement learning, the entropy of a policy, $\mathcal{H}(\pi(\cdot | s_i))$, represents the stochasticity of the policy at a given state s_i .⁵⁵⁻⁵⁷ The expression for this is given by:

$$\mathcal{H}(\pi(\cdot | s_i)) = - \sum_{a_i} \pi(a_i | s_i) \log \pi(a_i | s_i), \quad (6)$$

where $\pi(a_i | s_i)$ denotes the probability of taking action a_i in state s_i according to policy π . The policy is trained with the objective to maximize the expected return and the entropy at the same time:

$$\pi^* = \arg \max_{\pi} \sum_i \mathbb{E}_{(s_i, a_i) \sim \rho_{\pi}} [r(s_i, a_i) + \alpha \mathcal{H}(\pi(\cdot | s_i))], \quad (7)$$

where $\mathcal{H}(\cdot)$ is the entropy measure and the variable α functions as a temperature parameter that calibrates the relative significance of the entropy term against the reward, thereby modulating the stochasticity of the resulting optimal policy.^{56,58}

C. DRL-Enhanced Active Flow Control

We propose an interaction framework between the agent and the numerical simulation environment, where the agent observes the current state of the CFD environment and adjusts the mass flow rates of the two synthetic jets on the square cylinder based on reward feedback. This iterative optimization process enables the SAC agent to converge to an optimal flow control strategy. Moreover, the control objective of the DRL-based AFC framework is to reduce the lift and drag coefficients of the square cylinder while minimizing vortex shedding in the wake flow field.

The design of the DRL components is centered around this goal. The AFC problem is integrated with the DRL framework by defining three key components: the agent's action a_t (the mass flow rate of the synthetic jets), the agent's state s_t (observational data from the environment), and the agent's reward r_t (the control objectives). Firstly, the agent's action, defined as the mass flow rates of the synthetic jet, is limited to a mass flow rate not exceeding 2% of the upstream inflow. Furthermore, to ensure the smoothness of continuous actions, a smoothing function S is utilized between consecutive actions a_t and a_{t+1} , facilitating a gradual transition and mitigating abrupt changes in jet velocity. The smoothing function S is defined as follows:

$$S(V_{\Gamma_1, T_i}, a, V_{\Gamma_1, T_{i-1}}) = V_{\Gamma_1, T_i} + \beta \cdot (a - V_{\Gamma_1, T_{i-1}}), \quad (8)$$

where V_{Γ_1, T_i} is the updated value at time step i , V_{Γ_1, T_i} is the current value at time step i , a represents the target action magnitude a_t , $V_{\Gamma_1, T_{i-1}}$ is the value at the previous time step $i-1$, and β is a coefficient determining the extent of adjustment towards the target a . This function effectively interpolates between the previous value and the target action, with β controlling the smoothness of the transition.

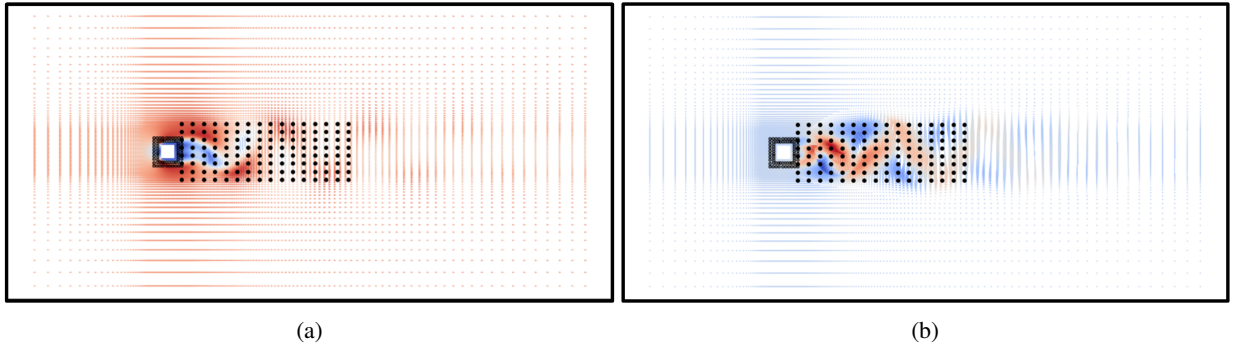


FIG. 6: Arrangement for probes position in flow around a square cylinder. (a) The probes are distributed in the instantaneous velocity field. (b) The probes are distributed in the pulsating velocity field.

Next, the state s_t represents the information observed by the agent from the environment. In this study, s_t is represented by physical information collected from specific locations within the computational domain. Specifically, 201 probes are placed around the square cylinder and in the wake region to capture instantaneous velocity or pressure data. The probes are strategically distributed to cover the area around the square cylinder, as one of the control objectives is to manage the lift and drag forces acting on the square cylinder. This necessitates the agent observing the physical field information in this region. Additionally, the probes are positioned to cover the recirculation zone in the cylinder's wake and capture areas with the highest fluctuating values, which is crucial for controlling the wake's instability. The specific distribution of the probes is illustrated in Fig. 6.

Moreover, the reward function is a core component of reinforcement learning. By incorporating C_D and C_L into the reward function, we align it with the primary objectives of reducing drag and suppressing lift. This reward function clearly defines the behaviors the agent should learn and drives the agent to seek optimal strategies through positive and negative feedback mechanisms that minimize drag and suppress lift. The specific reward function is defined as follows:

$$r_{T_i} = C_{D,0} - (C_D)_{T_i} - \omega |(C_L)_{T_i}|, \quad (9)$$

where $C_{D,0}$ represents the baseline drag coefficient C_D , serving as a reference point. $(C_D)_{T_i}$ denotes the drag coefficient at time step T_i , with the objective being to minimize this value relative to the baseline. $(C_L)_{T_i}$ denotes the lift coefficient at time step T_i . The parameter ω is a weight factor for the lift coefficient, typically ranging between 0.1 and 0.2.

During DRL training, each episode has a total duration of 1.25 seconds, including 100 training time steps. The control action is updated every 0.0125 seconds, equivalent to 25 numerical simulation time steps. Tested Reynolds numbers include 100 and 500, with vortex shedding periods approximately between 0.127 and 0.145 seconds. Therefore, an epoch is designed to last 1.25 seconds, corresponding to approximately 8.6 to 9.8 vortex shedding cycles. In each episode of DRL training, the CFD simulation spans multiple vortex shedding cycles, allowing the agent to observe flow characteristics over several shedding periods.

III. RESULTS

A. Baseline flow simulation

The state in which no flow control is applied is defined as the Baseline. In this study, active flow control begins from the baseline state, which also serves as a comparison to the controlled flow. As shown in Fig. 7 (a), at $Re = 100$, flow separation occurs near the leading edge corners of the square cylinder. Fig. 7 (b) provides a zoomed-in view of the flow around the square cylinder, where flow separation is observed near the leading edge corners, and recirculation bubbles form behind the cylinder. In this region, the fluid flows in the reverse direction, creating closed-loop circulation. In the wake region behind the cylinder, alternating vortex shedding occurs as the recirculation bubbles oscillate. When $Re = 500$, the vortex shedding pattern in the wake region of the square cylinder, as shown in Fig. 7 (c), differs from that at $Re = 100$. At this higher Reynolds number, the vortices behind the cylinder are no longer alternating and regular. In Fig. 7 (d), it can be observed that flow separation occurs near the leading edge corners, creating recirculation zones on both sides of the cylinder. Behind the cylinder, a fluctuating recirculation region forms, displaying oscillatory motion in the spanwise direction.

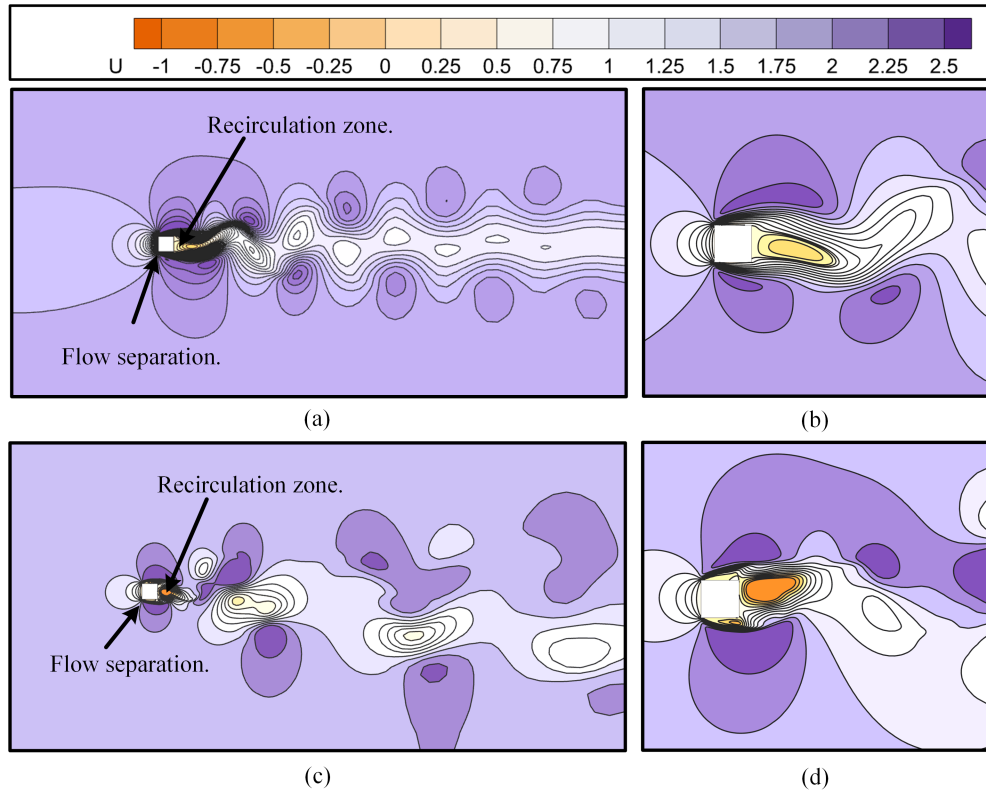
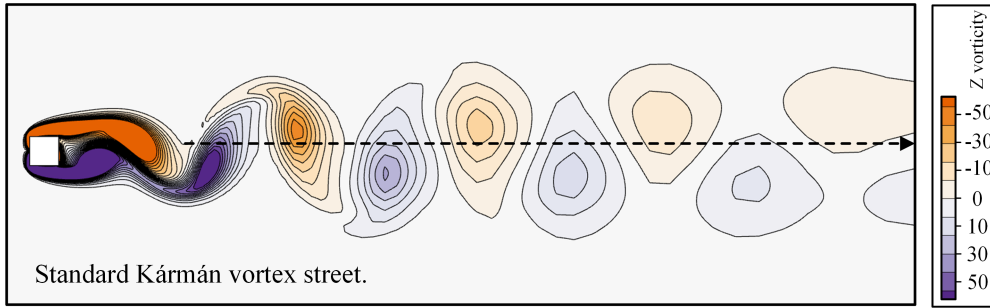
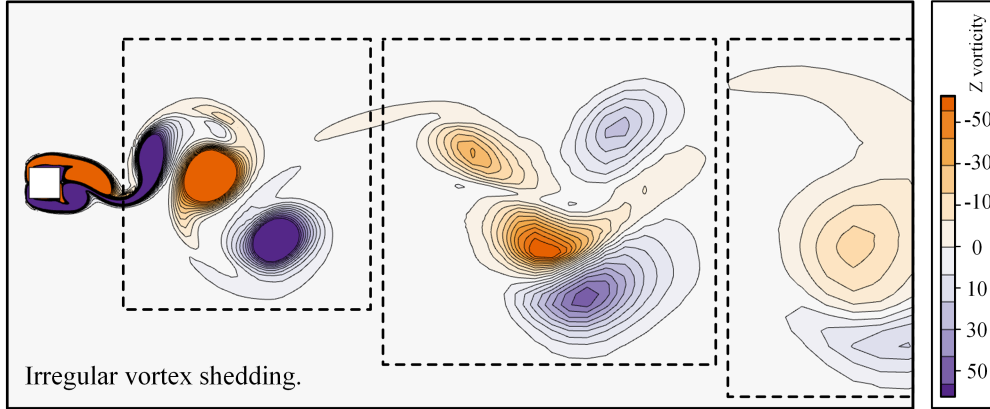


FIG. 7: Velocity magnitude of the flow around the square cylinder. (a) $Re = 100$, entire domain; (b) $Re = 100$, local domain; (c) $Re = 500$, entire domain; (d) $Re = 500$, local domain.

At $Re = 100$, the wake region of the square cylinder exhibits regular vortex shedding, as shown in Fig. 8. Vortices shed from the trailing edge of the cylinder form a regular pattern, characterized by alternating vortices along the centerline, creating a street-like structure. At $Re = 500$, the shedding pattern in the wake changes, as depicted in Fig. 9. After flow separation occurs at the leading edge of the square cylinder, some separated fluid reattaches to the cylinder surface. The vortex shedding in the wake region of the square cylinder becomes increasingly unstable, with vortices squeezing, stretching, and deforming as they develop downstream in the form of vortex pairs. Compared to $Re = 100$, the flow instability at $Re = 500$ intensifies, leading to a more complex shedding pattern in the wake. We have described the flow structures and vortex shedding patterns of the baseline flow at $Re = 100$ and $Re = 500$. At Reynolds number 500, the flow exhibits greater instability and complexity, indicating that the difficulty of flow control is increased. Implementing flow control techniques in such conditions requires advanced strategies that can effectively manipulate the flow dynamics and mitigate flow separation.

Next, we will present the base flow simulation of a semi-cylindrical body. The base flow represents the ideal state without vortex shedding and is used solely to calculate the drag coefficient in this idealized condition. This serves as an asymptote to measure the maximum possible drag reduction. The base flow corresponds to a stable equilibrium state of the controlled Navier-

FIG. 8: Snapshots of the spanwise vorticity field of the square cylinder wake at $Re = 100$.FIG. 9: Snapshots of the spanwise vorticity field of the square cylinder wake at $Re = 500$.

Stokes equations. In this state, the velocity and pressure fields of the fluid remain unchanged, constituting a stable solution of the Navier-Stokes equations. This state can be considered a potential fixed point in the configuration space of fluid flow. However, despite the apparent stability of the baseline flow, it is, in fact, unstable to infinitesimal perturbations, leading to the occurrence of vortex shedding phenomena. Vortex shedding is one of the sources of resistance experienced by the cylinder, and our active flow control aims to mitigate this resistance. Therefore, assessing the effectiveness of the control strategy can be done by using a modified baseline resistance value, assuming the absence of vortex shedding. To simulate the scenario without vortex shedding, the strategy involves simulating only the upper half of the computational domain along the centerline. Symmetric boundary conditions are applied at the lower boundary of the computational domain (where $y = 0$). These symmetric boundary conditions are explicitly defined as follows: the velocity component $v = 0$, and the derivatives of the velocity u and the pressure p with respect to y are zero, i.e., $\frac{\partial u}{\partial y} = 0$ and $\frac{\partial p}{\partial y} = 0$. The boundary conditions for the rest of the domain remain unchanged. This approach effectively models an idealized flow scenario.

In Fig. 10, simulations were performed for the cases of $Re = 100$ and $Re = 500$, where the wake flow behind the semi-square cylinder was in a steady state without vortex shedding, and the only reason for pressure drag was flow separation. The total drag coefficient encapsulates the intrinsic drag associated with the baseline flow and the correctable component, with only the second part of drag being adjustable through strategic manipulation of the von Kármán vortex shedding⁵⁹. We computed the asymptotic drag coefficients, denoted as C_{Dh} , for the semi-square cylinder at $Re = 100$ and $Re = 500$, which were found to be 0.668 and 0.498, respectively. These values were extended to obtain the baseline drag coefficients, denoted as C_{Db} , for a fully square cylinder in a steady-state flow, resulting in values of 1.335 and 0.995 for $Re = 100$ and $Re = 500$, respectively. The baseline drag coefficient, C_{Db} , will be compared with the drag obtained during active flow control to evaluate the effectiveness of the control strategy in reducing drag.

B. DRL-based control performance

In the Sec. III A, we have observed that the vortex shedding patterns are completely different at $Re = 100$ and $Re = 500$. This section primarily evaluates the performance of DRL-based AFC control at $Re = 100$ and $Re = 500$, focusing on its effectiveness in suppressing vortex shedding in the wake flow field, as well as its performance in drag reduction and lift suppression. The

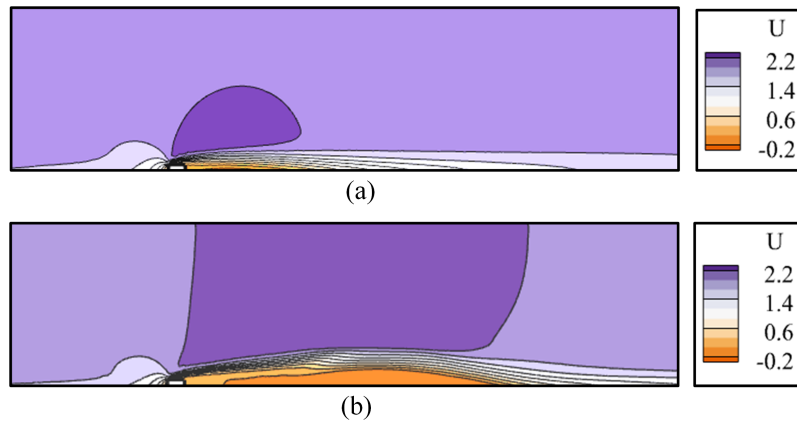


FIG. 10: The base flow is obtained through a simulation of a half-domain, where the x-coordinate ranges from $-10D$ to $30D$, and the y-coordinate ranges from 0 to $10D$. We apply symmetric boundary conditions on the $y = 0$ boundary, and the computational domain's mesh is consistent with Fig. 3. This configuration results in a scenario without vortex shedding, serving as a hypothetical baseline for comparison with the results of active flow control. (a) $Re = 100$; (b) $Re = 500$.

synthetic jets are positioned near the trailing edge corners of the square cylinder, with a width of $D/25$. In this section, we will evaluate the control performance of the DRL-based AFC technique at $Re = 100$ and $Re = 500$ separately. To visually observe the effect of vortex shedding suppression during the training process, Fig. 11 ($Re = 100$) and Fig. 12 ($Re = 500$) capture snapshots of the instantaneous velocity magnitude at four representative episodes on the learning curve. Then, we summarize the control performance in terms of drag reduction and lift suppression in Table. III. We also compare our trained results with other research studies for comparative analysis. By examining the control performance metrics and velocity magnitude snapshots, we can gain insights into the effectiveness of the DRL-based AFC technique in suppressing vortex shedding, reducing drag, and suppressing lift at $Re = 100$ and $Re = 500$.

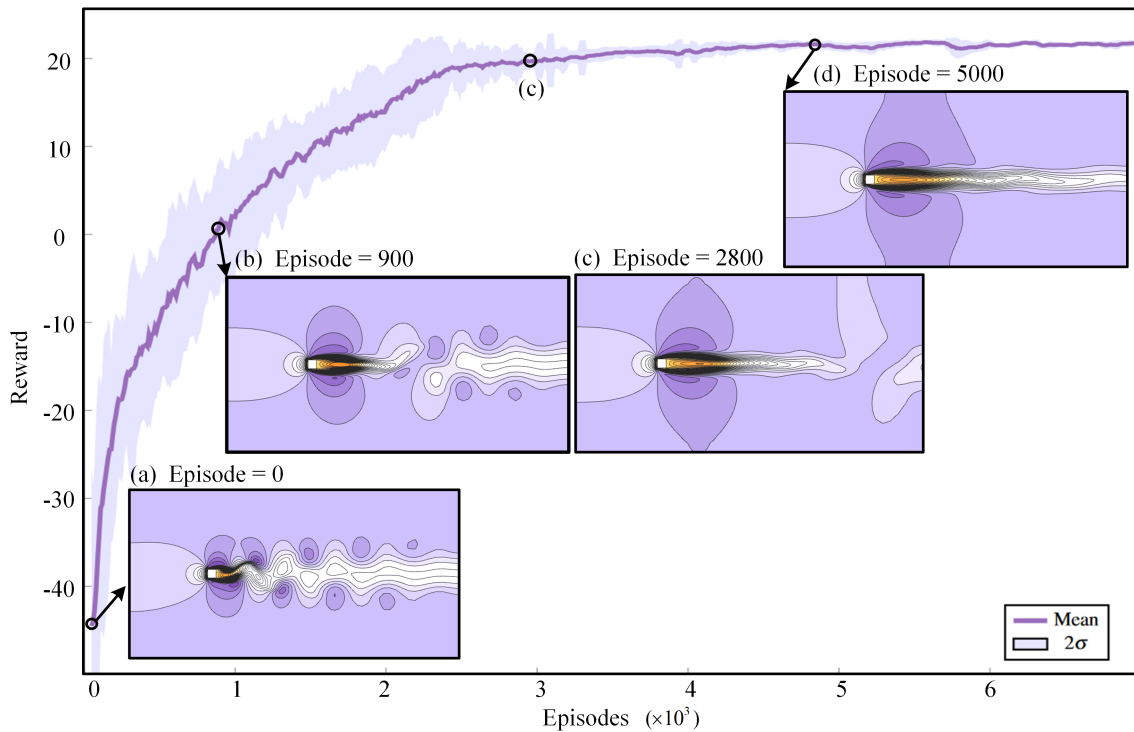


FIG. 11: When $Re = 100$, observed the evolution of the instantaneous velocity magnitude when DRL training. Specifically, focused on four key moments: (a) Episode = 0, (b) Episode = 900, (c) Episode = 2800, and (d) Episode = 5000.

For $Re = 100$, AFC is applied to the flow around a square cylinder using DRL, and the learning curve along with snapshots of the instantaneous velocity magnitude of the square cylinder are depicted in Fig. 11. The DRL training commences with the baseline flow field, characterized by alternating vortex shedding in the wake region. Flow control is then executed based on this initial condition. The cumulative reward function curve of the DRL training exhibits a sharp increase during the initial stages. After 900 episodes of training, the cumulative reward becomes positive, indicating that the PPO agent has discovered a control strategy that meets the objective function. At this point, the vortices generated in the wake region of the baseline flow field begin to move downstream, and the previously oscillating recirculation bubble behind the square cylinder is elongated. Although the recirculation bubble continues to oscillate, no new vortices are shed. As training progresses to 2800 episodes, the growth of the cumulative reward begins to level off, indicating that the DRL training is converging. By this stage, the flow field around the square cylinder has expelled the vortices that had shed in the baseline flow, with only the initial shed vortex continuing to move towards the outlet. After 5000 episodes of training, the cumulative reward reaches a plateau, signifying that the DRL training has stabilized and fully converged. At this point, vortex shedding in the wake region of the square cylinder is completely suppressed.

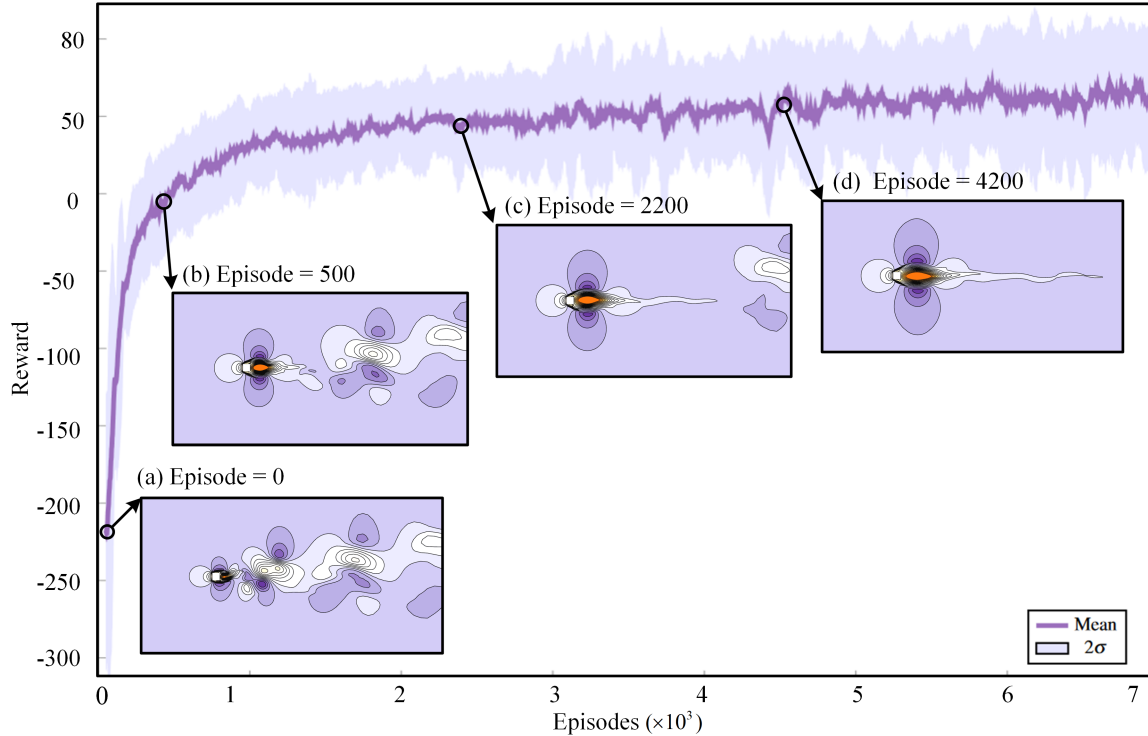


FIG. 12: When $Re = 500$, observed the evolution of the instantaneous velocity magnitude when DRL training. Specifically, focused on four key moments: (a) Episode = 0, (b) Episode = 500, (c) Episode = 2200, and (d) Episode = 4200.

Similarly, under a Reynolds number of 500, we employed DRL to execute active flow control around a square cylinder, with Fig. 12 depicting its learning curve and the instantaneous velocity magnitude during characteristic episodes. In the RL training process, the cumulative reward value of the first episode (R_0) is considered the starting point of the learning process. It is observed that at $Re = 500$, the R_0 of the DRL training is approximately -210, compared to -45 at $Re = 100$. Additionally, the initial stage's learning curve exhibits a steeper slope compared to the case of $Re = 100$. The significant difference indicates that at higher Reynolds numbers, the initial training phase faces more severe challenges and requires more extensive exploration to discover effective control strategies. In the first episode, the shedding of vortices in the wake of the baseline flow no longer follows a regular alternating pattern but evolves jointly as "vortex pairs". After 500 episodes of training, the cumulative reward has increased to a positive value, indicating that the PPO agent has explored effective control strategies that guide the reward function towards positivity. Currently, the recirculation area in the wake of the cylinder has enlarged and developed into an approximately symmetric and stable state. The two sets of vortices originally shed by the baseline flow gradually develop downstream in the computational domain, and at this point, no new vortices are shedding in the wake of the cylinder. As DRL training progresses to 2200 episodes, the growth rate of the learning curve slows down towards convergence. At this stage, the two sets of vortices shed by the baseline flow have been mostly expelled from the computational domain, with only some vortices still being shed from the outlet of the domain. Upon reaching 4200 episodes of training, the learning curve enters a plateau phase, and the reward function tends to converge. Furthermore, the recirculation area in the wake of the cylinder has stabilized to its maximum extent, and the phenomenon of vortex shedding has been completely suppressed.

C. Sensitivity analyses of synthetic jets

In the previous section, we observed the suppression process of vortex shedding in the wake of a square cylinder during DRL training at $Re = 100$ and $Re = 500$. The training results indicate that when the synthetic jets are positioned near the trailing edge corners of the square cylinder, DRL-based AFC can completely suppress vortex shedding in the wake at both $Re = 100$ and $Re = 500$. Additionally, Chen *et al.*⁴⁰ and Yan *et al.*⁴³ analyzed the impact of synthetic jet positioning on flow control efficacy, yielding some intriguing conclusions. Building on these findings, we integrate the optimization of jet actuator positioning with the optimization of feedback laws using DRL. This study tests Reynolds numbers of 100 and 500, representing two distinctly different vortex shedding modes. Firstly, we perform flow control using symmetric zero-mass-flux jets positioned at the leading and trailing edges of the square cylinder. The objective is to investigate how the positioning of jets actuators influences flow control performance. Secondly, we design synthetic jets with four different widths to study how the width of the synthetic jets affects flow control performance.

TABLE III: Impact of Synthetic Jets Actuator Placement on AFC Control Performance: Optimizing Position Selection.

Reference	Re	Jet Location	Suppress vortex	Mean C_D			Std of C_D			Std of C_L		
				$C_{D,Baseline}$	$C_{D,DRL}$	Reduction	$C_{D,Baseline}$	$C_{D,DRL}$	Reduction	$C_{L,Baseline}$	$C_{L,DRL}$	Reduction
Chen <i>et al.</i> ⁴⁰	100	Leading	NO	1.480	1.370	7.20	-	-	-	0.530	0.190	64.2
Chen <i>et al.</i> ⁴⁰	100	Trailing	YES	1.480	1.280	13.3	-	-	-	0.530	0.080	84.9
Our study	100	Leading	NO	1.549	1.353	12.7	2.020	0.001	99.9	0.179	0.033	81.5
Our study	100	Trailing	YES	1.549	1.325	14.4	2.020	0.001	99.9	0.179	0.025	86.1
Yan <i>et al.</i> ⁴³	500	Leading	NO	1.980	1.100	44.4	0.470	0.070	84.3	1.260	0.170	85.9
Yan <i>et al.</i> ⁴³	500	Trailing	NO	1.980	1.950	1.40	0.470	0.520	10.7	1.260	1.070	13.2
Our study	500	Leading	NO	2.060	0.711	65.5	0.440	0.268	86.7	1.173	0.650	44.4
Our study	500	Trailing	YES	2.060	1.001	51.4	0.441	0.042	90.5	1.173	0.294	74.9

As illustrated in Table. III, for $Re = 100$, positioning the synthetic jets near the leading edge of the square cylinder led to a 12.7% reduction in the average C_D compared to the baseline. The standard deviation of C_D was suppressed by 99.9%, and the standard deviation of the C_L was controlled by 81.5%. However, the wake remained unstable. This instability is evident in the oscillations observed in the C_D and C_L time history curves of the controlled flow, as depicted in Fig. 13. When the jets position are designed at the front corner points, the controlled flow exhibits significant reductions in both C_D and C_L compared to the baseline. However, when compared to the jet position designed at the trailing corner points, fluctuations in the C_D and C_L of the controlled flow still persist. When positioning the synthetic jets near the trailing edge of the square cylinder, a 14.4% decrease in the average C_D was observed compared to the baseline. The standard deviation of C_D was suppressed by 99.9%, and the standard deviation of the C_L was controlled by 93.1%. In addition, when the synthetic jets are positioned at the trailing edge corners of the square cylinder, the vortices in the controlled flow are completely suppressed, as detailed in Fig. 11. As shown in Fig. 13, the controlled flow exhibited a significant reduction in both C_D and C_L , with no fluctuations. Therefore, for $Re = 100$, positioning the synthetic jets near the trailing edge is advantageous for reducing the average C_D and fully suppressing vortex shedding. Chen *et al.*⁴⁰ obtained similar results at $Re = 100$, indicating that vortex shedding is completely suppressed only when the synthetic jets are positioned near the trailing edge of the square cylinder. Additionally, the reduction in C_D is more pronounced when synthetic jets are placed near the trailing edge.

In the case of $Re = 500$ in Table. III, when the synthetic jets are positioned near the front corner, the C_D reduction rate reaches 65.5%, with a decrease of 86.7% in the std of the C_D and a 44.4% reduction in the std of the C_L . When the synthetic jets are placed near the trailing corner, the C_D reduction rate is 51.4%, with a decrease of 90.5% in the std of the C_D and a 74.9% reduction in the std of the C_L . Therefore, when $Re = 500$, setting the position of the synthetic jet near the front corner point achieves a higher drag reduction rate than that near the trailing corner point. In the study by Yan *et al.*⁴³, it was similarly found that positioning the jets near the front corner points of the square cylinder is more advantageous for reducing the drag coefficient. Although positioning the synthetic jets near the leading corner results in a higher reduction rate of C_D , the flow stability of the controlled flow is stronger when the synthetic jets are positioned near the trailing corner. As shown in Fig. 13, both C_D and C_L in the controlled flow reach a stable state when the synthetic jets are placed near the trailing corner. On the contrary, when the synthetic jets are positioned near the leading corner, both C_D and C_L exhibit periodic oscillations.

As an illustration at $Re = 500$, we present the streamline visualizations for the baseline flow, controlled flow with the synthetic jets positioned near the leading edge, and controlled flow with the synthetic jets positioned near the trailing edge. Both the baseline and controlled flows represent the stable flow states attained after sufficient flow development. In Fig. 14, streamline plots are provided for these three scenarios, along with magnified views focusing on the flow patterns around the square cylinder. As shown in Fig. 14(a), flow separation occurs at the leading edge of the square cylinder in the baseline flow, forming recirculation regions on both sides of the cylinder, with significant oscillations in the wake flow streamlines. Fig. 14(b) illustrates the

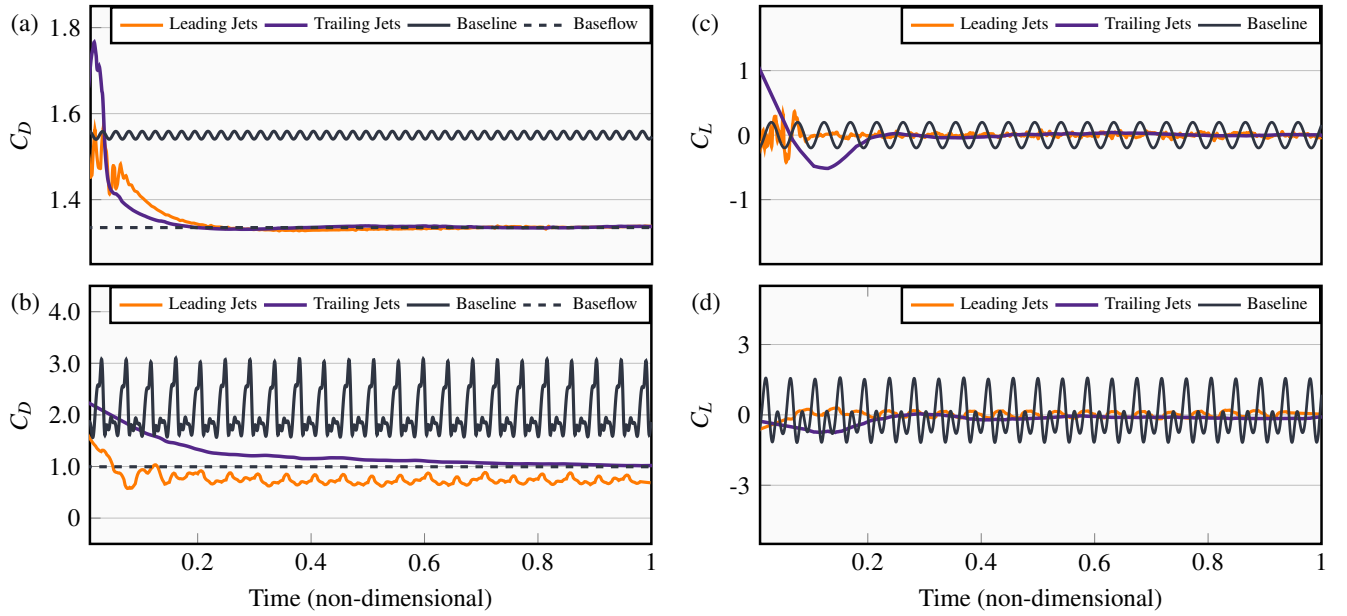


FIG. 13: Effect of synthetic jets positioning on flow control at $Re = 100$ and $Re = 500$. The leading jets are positioned near the front corners of the square cylinder, while the trailing jets are positioned near the trailing corner points. The precise locations of the synthetic jets are detailed in Fig. 2. (a) $Re = 100$, C_D ; (b) $Re = 100$, C_L ; (c) $Re = 500$, C_D ; (d) $Re = 500$, C_L .

streamlines around the square cylinder, along with separation bubbles near the sidewalls of the cylinder. Fig. 14(c) illustrates the stabilized flow field achieved after implementing control with the synthetic jets positioned near the leading edge of the square cylinder. In Fig. 14(d), the placement of the synthetic jets and the resulting streamlines around the cylinder are shown. On one side of the cylinder, the influence of the jet's blowing action enlarges the flow separation region, even forming a smaller separation bubble ahead of a larger one. Conversely, on the other side of the cylinder, the suction action of the jet creates a relatively smaller separation bubble near the leading corner. The separated flow near the leading edge quickly reattaches to the sidewall, undergoes flow separation again at the trailing edge, and sheds a vortex. Under the control of the synthetic jets, the near-field vortices continuously shed alternately, while the far-field wake gradually stabilizes.

Moreover, the synthetic jets are positioned near the trailing corner of the square cylinder, resulting in a stabilized wake flow after control in Fig. 14(e). Fig. 14(f) illustrates the placement of the synthetic jets and the streamlines around the square cylinder. Due to the influence of the synthetic jets, a stable and symmetric separation bubble forms on the leeward side of the cylinder, with minimal oscillation observed in the wake region's streamlines. Under the flow conditions at $Re = 500$, the stability of the controlled flow is effectively enhanced when the synthetic jets are positioned near the leading edge. When the synthetic jets are placed near the trailing edge, the controlled flow achieves a stable state without vortex shedding. In the work of Yan *et al.*⁴³, the DRL control framework they designed focuses on reducing C_D and C_L , and the control strategy produces obvious control effects at multiple Reynolds numbers. In our research, we not only focus on reducing the lift and drag coefficients, but also on controlling the stability of the wake region and the detachment of the vortex behind the square cylinder. The control strategy we obtained completely suppresses the shedding of vortices in the square cylinder wake area under the flow of $Re = 500$. This discrepancy arises because, in our research, the agent is capable of observing not only the flow field information around the square cylinder but also, more importantly, the flow field information in the most pulsating regions of the wake field. Li and Zhang²⁹ employed a similar probe design approach and developed a control strategy capable of completely suppressing the Kármán vortex street phenomenon in the wake field of a cylinder.

To comprehensively illustrate the control process of synthetic jets positioned near the front and trailing corner points on the wake flow field around a square cylinder, we present the case of $Re = 500$. We display the contours of instantaneous vorticity from the initiation to the ending of the control process. Initially, the activation of the synthetic jets affects only the flow near the square cylinder. We focus on this region initially, and as the control progresses, the influence extends to the wake field, ultimately showcasing the instantaneous vorticity values across the entire computational domain. When the synthetic jets are positioned near the leading edge of the square cylinder, the evolution of the instantaneous vorticity field during the control process is described using five representative time snapshots, as depicted in Fig. 15. In Fig. 15(a), the control action initiates near the leading edge of the square cylinder, causing a slight disruption in the originally continuous vorticity field. Moving to Fig. 15(b), as the synthetic jets near the leading edge continue their control action, their influence on the vorticity around the square cylinder gradually extends rearward. By the time Fig. 15(c) is reached, vortices generated from flow separation near the

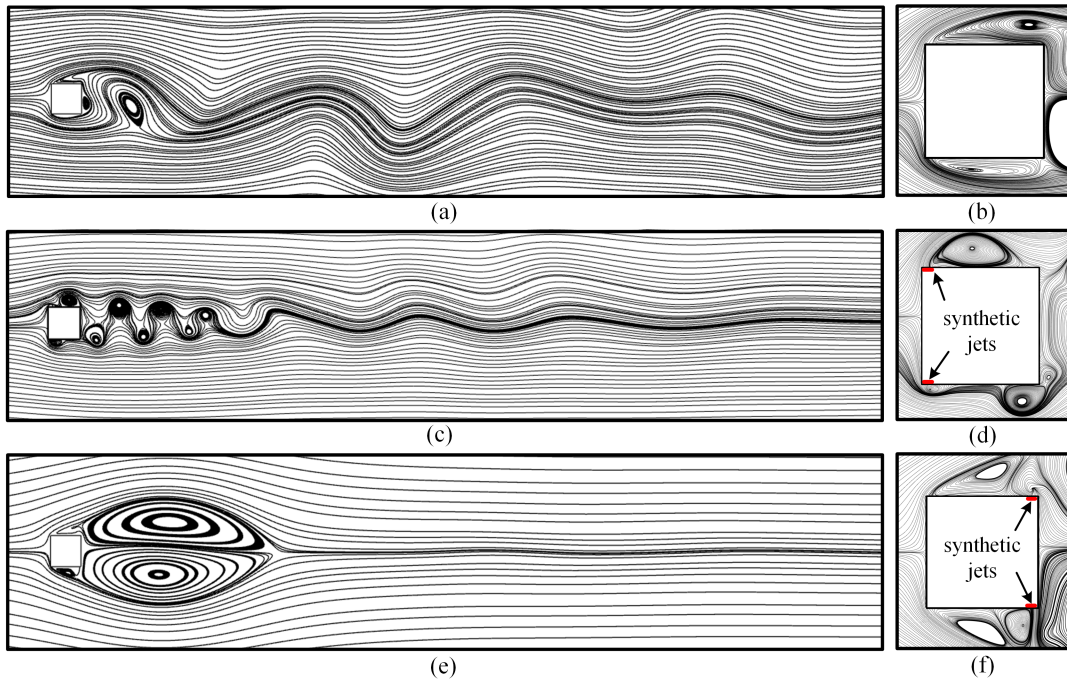


FIG. 14: At $Re = 500$, the visualizations depict streamlines under various configurations: baseline flow, the controlled flow with the synthetic jets near the leading edge, and synthetic jets near the trailing edge. Specifically: (a) and (b) for Baseline flow. (c) and (d) for the controlled flow with the synthetic jets positioned near the leading edge. (e) and (f) for the controlled flow with the synthetic jets positioned near the trailing edge.

leading edge reattach to the cylinder's sidewalls, elongating along the walls towards the rear corner of the cylinder. As the flow control progresses to Fig. 15(d), the originally continuous large vortex around the cylinder was disrupted and divided into several smaller vortices. These smaller vortices developed towards the rear corner, and after separating again, formed alternating vortex shedding in the wake region. When the synthetic jets were located near the leading edge of the square cylinder, after the flow control reached a stable state in Fig. 15(e), alternating vortex shedding occurred on the leeward side of the cylinder, and the shed vortices gradually dissipated in the far field due to the dissipation effect.

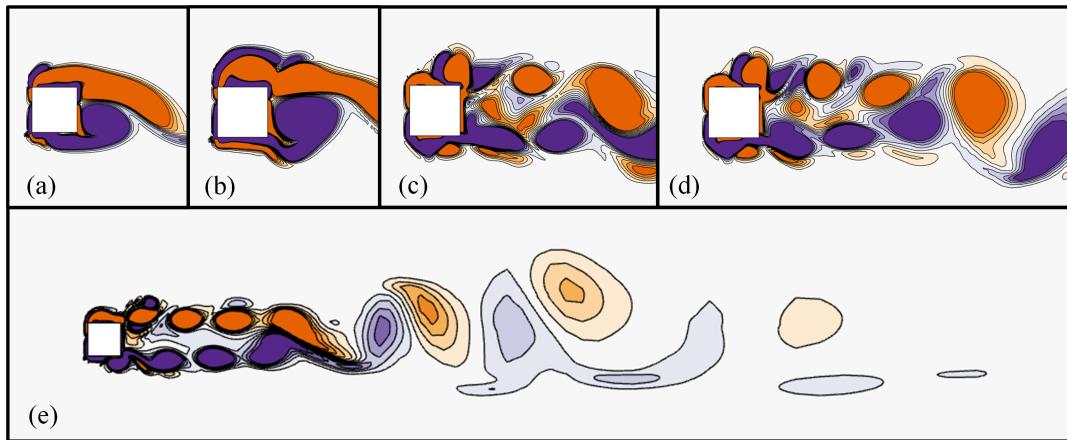


FIG. 15: At $Re = 500$, the instantaneous vorticity at characteristic moments during the control process are displayed for synthetic jets positioned near the leading corner points of the square cylinder. (a) t_1 ; (b) t_2 ; (c) t_3 ; (d) t_4 ; (e) t_5 .

When the synthetic jets are positioned near the trailing edge of the square cylinder, as shown in Fig. 16(a), the control process begins with one side of the square cylinder initiating a suction action while the other side performs a blowing action. In Fig. 16(b), at time t_1 , the control action disrupts the vorticity field downstream, and by Fig. 16(c), a new pair of vortices has formed downstream of the square cylinder. The originally periodic oscillation of positive and negative vortices on the trailing

side of the square cylinder gradually develops into a symmetrical pattern under the influence of the synthetic jets, as depicted in Fig. 16(d). In Fig. 16(e), as the flow control progresses to its conclusion, the recirculation region on the backside of the square cylinder appears symmetrical and stable, with the phenomenon of vortex shedding completely suppressed in the wake flow field.

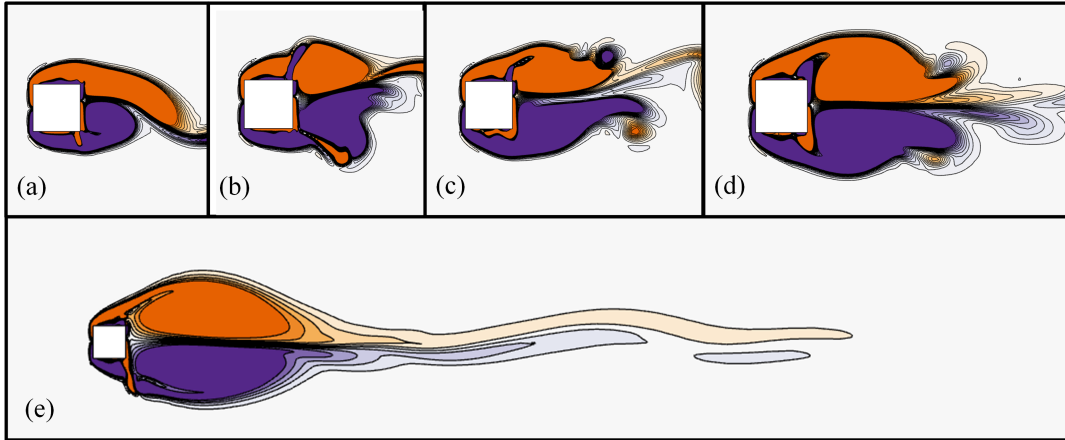


FIG. 16: At $Re = 500$, the instantaneous vorticity at characteristic moments during the control process are displayed for synthetic jets positioned near the trailing corner points of the square cylinder. (a) t_1 ; (b) t_2 ; (c) t_3 ; (d) t_4 ; (e) t_5 .

Next, we will investigate the impact of synthetic jets width on flow control performance. To achieve the complete suppression of vortices in the wake flow, we position the synthetic jets near the trailing corner of the square cylinder. The width of the synthetic jets under study ranges from $D/20$, $D/25$, $D/30$ to $D/35$, where D represents the characteristic dimension of the square cylinder. Performance metrics for flow control include the reduction rate of the average drag coefficient, and the standard deviations of lift and drag coefficients, as well as the average and standard deviation of action. The stability of training results is evaluated using the standard deviations of C_D , C_L , and action. We conduct experiments under two flow conditions, $Re = 100$ and $Re = 500$, to test the training results for the four jet widths. The summarized performance metrics are presented in Table. IV, and the time-history curves of C_D , C_L , and action are illustrated in Fig. 17.

TABLE IV: Impact of Synthetic Jets Width on AFC Control Performance: Optimizing Width Selection.

Re	Jet Width	Mean C_D			Std of C_D			Std of C_L			Action	
		$C_{D,Baseline}$	$C_{D,DRL}$	Reduction	$C_{D,Baseline}$	$C_{D,DRL}$	Reduction	$C_{L,Baseline}$	$C_{L,DRL}$	Reduction	Action Mean	Action Std
100	D/20	1.549	1.346	13.1	2.020	0.001	99.9	0.179	0.028	84.3	-0.016	0.146
100	D/25	1.549	1.325	14.4	2.020	0.001	99.9	0.179	0.025	86.1	0.037	0.164
100	D/30	1.549	1.345	13.2	2.020	0.003	99.9	0.179	0.037	79.0	0.063	0.316
100	D/35	1.549	1.314	15.2	2.020	0.001	99.9	0.179	0.056	68.5	0.072	0.290
500	D/20	2.060	1.021	50.4	0.441	0.023	94.8	1.173	0.186	84.2	-0.384	1.048
500	D/25	2.060	1.001	51.4	0.441	0.042	90.5	1.173	0.294	74.9	-0.702	1.223
500	D/30	2.060	0.968	53.0	0.441	0.080	81.8	1.173	0.291	75.2	-2.068	1.857
500	D/35	2.060	1.053	48.9	0.441	0.219	50.3	1.173	0.583	50.3	-0.789	4.333

a. $C_{D,Baseline}$ represents the time-averaged drag coefficient of the square cylinder when the baseline flow is fully developed.

b. $C_{D,DRL}$ represents the time-averaged drag coefficient of the square cylinder after AFC based on DRL.

c. The reduction is used to quantify the reduction ratio of the DRL control result relative to the baseline, expressed in percentage (%).

d. Action represents the ratio of the mass flow rate of the synthetic jets to the flow rate from the inlet.

Table. IV presents the results of training the jets at four different widths. At $Re = 100$, the average drag coefficient reduction ranges from 13.1% to 15.2% as the width of the synthetic jets transitions from $D/20$, $D/25$, $D/30$ to $D/35$, with the standard deviations of the C_D all approaching 99.9%. The impact on the drag reduction rate and the stability of the C_D is minor across the four widths of the synthetic jets. However, the reduction in the standard deviation of the C_L under $D/30$ and $D/35$ widths is smaller than that under $D/20$ and $D/25$. Further reduction in the width of the synthetic jets adversely affects the stability of the C_L . The average and standard deviation of actions are greater under $D/30$ and $D/35$ compared to $D/20$ and $D/25$. Decreasing the width of the synthetic jets leads to an increase in both the average and standard deviation of actions utilized. This shows that as the jet width decreases, the control system requires larger amplitude and varying range of actions to achieve the same control effect. At $Re = 500$, the reduction rate in the average drag coefficient ranges from 48.9% to 53.0%, with the width of the

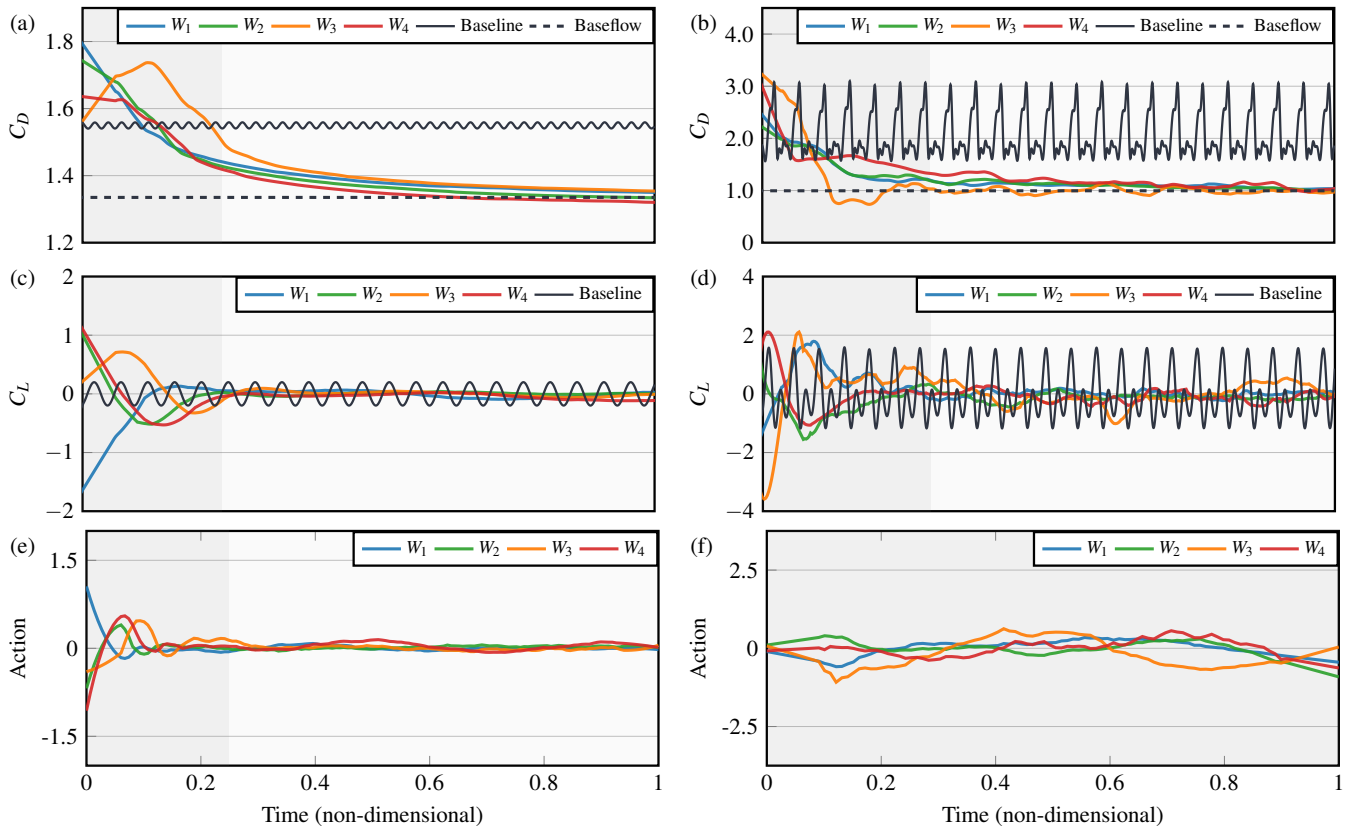


FIG. 17: Effect of synthetic jets width on flow control, for $Re = 100$ and $Re = 500$. W_1 , W_2 , W_3 , and W_4 represent jet widths of $D/20$, $D/25$, $D/30$, and $D/35$, respectively. (a) $Re = 100$, C_D ; (b) $Re = 500$, C_D ; (c) $Re = 100$, C_L ; (d) $Re = 500$, C_L ; (e) $Re = 100$, Action; (f) $Re = 500$, Action.

synthetic jets having minimal impact on the drag reduction rate. However, the reduction rates in the standard deviations of the C_D and C_L decrease with decreasing width of the synthetic jets. Additionally, the average value and standard deviation of action show consistency with $Re = 100$, where narrowing the width of the synthetic jets results in an increase in both the average value and standard deviation of action.

The time curves of C_D , C_L , and control actions for the square cylinder at $Re = 100$ and $Re = 500$ are depicted in Fig. 17. For the $Re = 100$ case, at four different synthetic jets widths, the initial stages show significant fluctuations in C_D , C_L , and control actions. After this period of intense fluctuation, C_L and control actions stabilize near zero, while C_D stabilizes near its minimum value. Upon observing the stabilized results, it is evident that the width of the synthetic jets has a minimal impact on drag reduction, although narrower jet widths adversely affect the stability of C_L and control actions. In the case of $Re = 500$, C_D , C_L , and control actions also experience significant fluctuations during the initial stages across all four synthetic jets widths. However, the stability of C_D , C_L , and control actions is generally worse compared to the $Re = 100$ case. This is attributed to the inherently more unstable flow field at $Re = 500$, making control more challenging. Comparing the control results for different synthetic jets widths, further narrowing the jet width has a more significant negative impact on the stability of C_D , C_L , and control actions.

IV. CONCLUSIONS

In this study, we investigate the application of DRL-based AFC in mitigating the lift and drag coefficients of a square cylinder while suppressing vortex shedding in the wake field. We design an interaction framework between the agent and a numerical simulation environment, optimizing its control strategy through learning and trial-and-error. The agent observes the state information of the numerical simulation environment and adjusts the mass flow rates of two synthetic jets on the square cylinder based on feedback from reward signals. Through an iterative optimization process, the SAC agent gradually converges towards the optimal flow control strategy, achieving multiple control objectives such as reducing lift and drag coefficients and suppressing vortex shedding. We will evaluate the performance of the SAC agent in controlling synthetic jets on a square cylinder for active flow control, and further analyze the impact of the position and width of the synthetic jet actuators on flow control effectiveness.

The main findings of this study can be summarized as follows:

Placing the synthetic jets at both the leading and trailing edge corners significantly reduces the lift and drag coefficients of the square cylinder. However, complete suppression of vortices in the wake field, along with more stable lift and drag coefficients, is only achieved when the synthetic jets are positioned near the trailing edge corners. When the synthetic jets are located at the trailing edge corners, at $Re = 100$, the mean drag coefficient decreases by 14.4%, the standard deviation of the drag coefficient reduces by 99%, and the standard deviation of the lift coefficient decreases by 86.1%. Additionally, the vortices in the wake field of the baseline flow are completely suppressed, with no new vortices shedding. At $Re = 500$, the mean drag coefficient decreases by 51.4%, the standard deviation of the drag coefficient reduces by 90.5%, and the standard deviation of the lift coefficient decreases by 74.9%. Similarly, the vortices shed in the wake field of the baseline flow are entirely suppressed. Although there is still slight instability in the wake field, no new vortices shed downstream of the square cylinder.

Additionally, we designed four different jet widths with the synthetic jets positioned at the trailing edge corners. The DRL training results indicate that at $Re = 100$, with jet widths of $D/20$, $D/25$, $D/30$, and $D/35$, the mean drag coefficient decreases by 13.1%, 14.4%, 13.2%, and 15.2%, respectively. The standard deviation of the drag coefficient reduces by 99% across all widths, while the standard deviation of the lift coefficient decreases by 84.3%, 86.1%, 79.0%, and 68.5%, respectively. This shows that DRL-based AFC effectively reduces both drag and lift coefficients across all jet widths, although narrower jet widths result in more unstable training outcomes, with higher means and standard deviations of the action. At $Re = 500$, with jet widths of $D/20$, $D/25$, $D/30$, and $D/35$, the mean drag coefficient decreases by 50.4%, 51.4%, 53.0%, and 48.9%, respectively. The standard deviation of the drag coefficient reduces by 94.8%, 90.5%, 81.8%, and 50.3%, while the standard deviation of the lift coefficient decreases by 84.2%, 74.9%, 75.2%, and 50.3%, respectively. These results demonstrate that both drag and lift coefficients are effectively reduced across all jet widths. However, the reduction rates of the standard deviations for C_D , C_L , and the action decrease as the synthetic jets width narrows. When AFC uses narrower synthetic jets, the stability of the controlled flow's C_D , C_L , and action is poorer. This study provides valuable references for the width and position of zero-net mass flux-driven synthetic jets, offering guidance for the practical application of DRL-based active flow control of square cylinders.

ACKNOWLEDGMENTS

The authors would like to express their gratitude to Dr. Jean Rabault (University of Oslo, Oslo, Norway), Dr. Jichao Li (National University of Singapore, Singapore), and Mr. Qiulei Wang (The University of Hong Kong, Hong Kong SAR, China) for making their open-source codes for deep reinforcement learning and numerical simulation available online. These resources have significantly contributed to the research presented in this paper. The relevant code repositories can be accessed at <https://github.com/jerabaul29/Cylinder2DFlowControlDRLParallel>^{26,60}, https://github.com/npuljc/RL_control_Nek5000^{29,61}, and <https://github.com/venturi123/DRLinFluids>^{33,62}.

AUTHOR DECLARATIONS

A. Conflict of Interest

The authors report no conflict of interest.

B. Author Contributions

DATA AVAILABILITY

The data that support the findings of this study are available from the corresponding author upon reasonable request.

AUTHOR ORCIDS

Wang Jia <https://orcid.org/0009-0008-2786-397X>
 Hang Xu <https://orcid.org/0000-0003-4176-0738>.

REFERENCES

- ¹S. L. Brunton, B. R. Noack, and P. Koumoutsakos, “Machine learning for fluid mechanics,” *Annual Review of Fluid Mechanics* **52**, 477–508 (2020).
- ²B. Mahesh, “Machine learning algorithms-a review,” *International Journal of Science and Research (IJSR)*. [Internet] **9**, 381–386 (2020).
- ³K. Manohar, B. W. Brunton, J. N. Kutz, and S. L. Brunton, “Data-driven sparse sensor placement for reconstruction: Demonstrating the benefits of exploiting known patterns,” *IEEE Control Systems Magazine* **38**, 63–86 (2018).
- ⁴P. Perdikaris, D. Venturi, and G. E. Karniadakis, “Multifidelity information fusion algorithms for high-dimensional systems and massive data sets,” *SIAM Journal on Scientific Computing* **38**, B521–B538 (2016).
- ⁵T. R. Bewley, P. Moin, and R. Temam, “Dns-based predictive control of turbulence: An optimal benchmark for feedback algorithms,” *Journal of Fluid Mechanics* **447**, 179–225 (2001).
- ⁶L. N. Cattafesta and M. Sheplak, “Actuators for active flow control,” *Annual Review of Fluid Mechanics* **43**, 247–272 (2011).
- ⁷S. Aram, Y.-T. Lee, H. Shan, and A. Vargas, “Computational fluid dynamic analysis of fluidic actuator for active flow control applications,” *AIAA Journal* **56**, 111–120 (2018).
- ⁸A. Glezer and M. Amitay, “Synthetic jets,” *Annual Review of Fluid Mechanics* **34**, 503–529 (2002).
- ⁹M. Jahanmiri, “Active flow control: a review,” *Flow Measurement and Instrumentation* **21**, 7–28 (2010).
- ¹⁰B. L. Smith and A. Glezer, “The formation and evolution of synthetic jets,” *Physics of Fluids* **10**, 2281–2297 (1998).
- ¹¹V. François-Lavet, P. Henderson, R. Islam, M. G. Bellemare, and J. Pineau, “An introduction to deep reinforcement learning,” *Foundations and Trends® in Machine Learning* **11**, 219–354 (2018).
- ¹²F. Xie, C. Zheng, T. Ji, X. Zhang, R. Bi, H. Zhou, and Y. Zheng, “Deep reinforcement learning: A new beacon for intelligent active flow control,” *Aerospace Research Communications* **1** (2023), 10.3389/arc.2023.11130.
- ¹³S. Scott Collis, R. D. Joslin, A. Seifert, and V. Theofilis, “Issues in active flow control: theory, control, simulation, and experiment,” *Progress in Aerospace Sciences* **40**, 237–289 (2004).
- ¹⁴B. Smith and G. Swift, “A comparison between synthetic jets and continuous jets,” *Experimental Fluids* **34**, 467–472 (2003).
- ¹⁵S. L. Brunton and B. R. Noack, “Closed-loop turbulence control: Progress and challenges,” *ASME Applied Mechanics Reviews* **67**, 050801 (2015).
- ¹⁶D. M. Luchtenburg, “Data-driven science and engineering: machine learning, dynamical systems, and control (brunton, steven l. and kutz, j. nathan; 2020 [bookshelf],” *IEEE Control Systems Magazine* **41**, 95–102 (2021).
- ¹⁷S. L. Brunton, J. L. Proctor, and J. N. Kutz, “Discovering governing equations from data by sparse identification of nonlinear dynamical systems,” *Proceedings of the National Academy of Sciences* **113**, 3932–3937 (2016).
- ¹⁸V. Mnih, K. Kavukcuoglu, D. Silver, A. Graves, I. Antonoglou, D. Wierstra, and M. Riedmiller, “Playing atari with deep reinforcement learning,” (2013), arXiv:1312.5602 [cs.LG].
- ¹⁹Y. LeCun, Y. Bengio, and G. Hinton, “Deep learning,” *Nature* **521**, 436–444 (2015).
- ²⁰V. Mnih, K. Kavukcuoglu, D. Silver, *et al.*, “Human-level control through deep reinforcement learning,” *Nature* **518**, 529–533 (2015).
- ²¹T. P. Lillicrap, J. J. Hunt, A. Pritzel, N. Heess, T. Erez, Y. Tassa, D. Silver, and D. Wierstra, “Continuous control with deep reinforcement learning,” (2019), arXiv:1509.02971 [cs.LG].
- ²²P. Henderson, R. Islam, P. Bachman, J. Pineau, D. Precup, and D. Meger, “Deep reinforcement learning that matters,” (2019), arXiv:1709.06560 [cs.LG].
- ²³Y. Li, “Deep reinforcement learning: An overview,” (2018), arXiv:1701.07274 [cs.LG].
- ²⁴L. Kaiser, M. Babaeizadeh, P. Milos, B. Osinski, R. H. Campbell, K. Czechowski, D. Erhan, C. Finn, P. Kozakowski, S. Levine, A. Mohiuddin, R. Sepassi, G. Tucker, and H. Michalewski, “Model-based reinforcement learning for atari,” (2024), arXiv:1903.00374 [cs.LG].
- ²⁵K. Arulkumar, M. P. Deisenroth, M. Brundage, and A. A. Bharath, “Deep reinforcement learning: A brief survey,” *IEEE Signal Processing Magazine* **34**, 26–38 (2017).
- ²⁶J. Rabault, M. Kuchta, A. Jensen, U. Réglade, and N. Cerardi, “Artificial neural networks trained through deep reinforcement learning discover control strategies for active flow control,” *Journal of fluid mechanics* **865**, 281–302 (2019).
- ²⁷H. Tang, J. Rabault, A. Kuhnle, Y. Wang, and T. Wang, “Robust active flow control over a range of Reynolds numbers using an artificial neural network trained through deep reinforcement learning,” *Physics of Fluids* **32**, 053605 (2020).
- ²⁸R. Paris, S. Beneddine, and J. Dandois, “Robust flow control and optimal sensor placement using deep reinforcement learning,” *Journal of Fluid Mechanics* **913**, A25 (2021).
- ²⁹J. Li and M. Zhang, “Reinforcement-learning-based control of confined cylinder wakes with stability analyses,” *Journal of Fluid Mechanics* **932**, A44 (2022), 2111.07498 [physics].
- ³⁰D. Fan, L. Yang, Z. Wang, M. S. Triantafyllou, and G. E. Karniadakis, “Reinforcement learning for bluff body active flow control in experiments and simulations,” *Proceedings of the National Academy of Sciences* **117**, 26091–26098 (2020).
- ³¹J. Rabault and A. Kuhnle, “Accelerating deep reinforcement learning strategies of flow control through a multi-environment approach,” *Physics of Fluids* **31**, 094105 (2019).
- ³²W. Jia and H. Xu, “Optimal parallelization strategies for active flow control in deep reinforcement learning-based computational fluid dynamics,” (2024), arXiv:2402.11515 [cs.LG].
- ³³Q. Wang, L. Yan, G. Hu, C. Li, Y. Xiao, H. Xiong, J. Rabault, and B. R. Noack, “DRLinFluids: An open-source Python platform of coupling deep reinforcement learning and OpenFOAM,” *Physics of Fluids* **34**, 081801 (2022).
- ³⁴R. Castellanos, G. Y. Cornejo Maceda, I. de la Fuente, B. R. Noack, A. Ianiro, and S. Discetti, “Machine-learning flow control with few sensor feedback and measurement noise,” *Physics of Fluids* **34**, 047118 (2022).
- ³⁵W. Jia and H. Xu, “Deep reinforcement learning-based active flow control of an elliptical cylinder: Transitioning from an elliptical cylinder to a circular cylinder and a flat plate,” (2024), arXiv:2404.13003 [physics.flu-dyn].
- ³⁶F. Ren, C. Wang, and H. Tang, “Bluff body uses deep-reinforcement-learning trained active flow control to achieve hydrodynamic stealth,” *Physics of Fluids* **33**, 093602 (2021).
- ³⁷X.-J. He, Y.-Z. Wang, Y. Hua, Z.-H. Chen, Y.-B. Li, and W.-T. Wu, “Policy transfer of reinforcement learning-based flow control: From two- to three-dimensional environment,” *Physics of Fluids* **35**, 055116 (2023).
- ³⁸H. Tang, J. Rabault, A. Kuhnle, Y. Wang, and T. Wang, “Robust active flow control over a range of Reynolds numbers using an artificial neural network trained through deep reinforcement learning,” *Physics of Fluids* **32**, 053605 (2020).
- ³⁹F. Ren, J. Rabault, and H. Tang, “Applying deep reinforcement learning to active flow control in turbulent conditions,” *Physics of Fluids* **33**, 037121 (2021), 2006.10683 [physics].

- ⁴⁰W. Chen, Q. Wang, L. Yan, G. Hu, and B. R. Noack, “Deep reinforcement learning-based active flow control of vortex-induced vibration of a square cylinder,” *Physics of Fluids* **35**, 053610 (2023).
- ⁴¹C. Xia, J. Zhang, E. Kerrigan, and G. Rigas, “Active flow control for bluff body drag reduction using reinforcement learning with partial measurements,” *Journal of Fluid Mechanics* **981**, A17 (2024).
- ⁴²W. Jia and H. Xu, “Robust and adaptive deep reinforcement learning for enhancing flow control around a square cylinder with varying reynolds numbers,” (2024), arXiv:2404.12123 [physics.flu-dyn].
- ⁴³L. Yan, Y. Li, G. Hu, W.-l. Chen, W. Zhong, and B. R. Noack, “Stabilizing the square cylinder wake using deep reinforcement learning for different jet locations,” *Physics of Fluids* **35**, 115104 (2023).
- ⁴⁴H. Bai and M. M. Alam, “Dependence of square cylinder wake on reynolds number,” *Physics of Fluids* **30**, 015102 (2018).
- ⁴⁵D.-H. Yoon, K.-S. Yang, and C.-B. Choi, “Flow past a square cylinder with an angle of incidence,” *Physics of Fluids* **22**, 043603 (2010).
- ⁴⁶S. Sen, S. Mittal, and G. Biswas, “Flow past a square cylinder at low reynolds numbers,” *Int. J. Numer. Meth. Fluids* **67**, 1160–1174 (2011).
- ⁴⁷L. Yan, Y. Li, B. Liu, and G. Hu, “Aerodynamic force reduction of rectangular cylinder using deep reinforcement learning-controlled multiple jets,” *Physics of Fluids* **36**, 025169 (2024).
- ⁴⁸H. Jasak, A. Jemcov, Z. Tukovic, *et al.*, “Openfoam: A c++ library for complex physics simulations,” in *International Workshop on Coupled Methods in Numerical Dynamics*, Vol. 1000 (2007) pp. 1–20.
- ⁴⁹H. Jasak, “OpenFOAM: Open source CFD in research and industry,” *International Journal of Naval Architecture and Ocean Engineering* **1**, 89–94 (2009).
- ⁵⁰A. Sharma and V. Eswaran, “Heat and fluid flow across a square cylinder in the two-dimensional laminar flow regime,” *Numerical Heat Transfer, Part A: Applications* **45**, 247–269 (2004).
- ⁵¹A. P. Singh, A. K. De, V. K. Carpenter, V. Eswaran, and K. Muralidhar, “Flow past a transversely oscillating square cylinder in free stream at low reynolds numbers,” *International Journal for Numerical Methods in Fluids* **61**, 658–682 (2009).
- ⁵²S. Cao, Y. Ge, and Y. Tamura, “Shear effects on flow past a square cylinder at moderate reynolds numbers,” *Journal of Engineering Mechanics* **138**, 116–123 (2012).
- ⁵³H. Bai and M. M. Alam, “Dependence of square cylinder wake on Reynolds number,” *Physics of Fluids* **30**, 015102 (2018).
- ⁵⁴A. Sohankar, C. Norberg, and L. Davidson, “Simulation of three-dimensional flow around a square cylinder at moderate Reynolds numbers,” *Physics of Fluids* **11**, 288–306 (1999).
- ⁵⁵T. Haamoja, A. Zhou, P. Abbeel, and S. Levine, “Soft actor-critic: Off-policy maximum entropy deep reinforcement learning with a stochastic actor,” (2018), arXiv:1801.01290 [cs.LG].
- ⁵⁶T. Haamoja, A. Zhou, P. Abbeel, and S. Levine, “Soft actor-critic: Off-policy maximum entropy deep reinforcement learning with a stochastic actor,” in *Proceedings of the 35th International Conference on Machine Learning*, Proceedings of Machine Learning Research, Vol. 80, edited by J. Dy and A. Krause (PMLR, 2018) pp. 1861–1870.
- ⁵⁷T. Haamoja, A. Zhou, K. Hartikainen, G. Tucker, S. Ha, J. Tan, V. Kumar, H. Zhu, A. Gupta, P. Abbeel, and S. Levine, “Soft actor-critic algorithms and applications,” (2019), arXiv:1812.05905 [cs.LG].
- ⁵⁸T. Haamoja, A. Zhou, K. Hartikainen, G. Tucker, S. Ha, J. Tan, V. Kumar, H. Zhu, A. Gupta, P. Abbeel, and S. Levine, “Soft actor-critic algorithms and applications,” (2019), arXiv:1812.05905 [cs.LG].
- ⁵⁹B. Protas and J. E. Wesfreid, “Drag force in the open-loop control of the cylinder wake in the laminar regime,” *Physics of Fluids* **14**, 810–826 (2002).
- ⁶⁰J. Rabault and A. Kuhnle, “Cylinder2dflowcontroldrparallel,” GitHub. <https://github.com/jerabaul29/Cylinder2DFlowControlDRLParallel> (2019).
- ⁶¹J. Li, “Rlcontrolnek5000,” GitHub. https://github.com/npuljc/RL_control_Nek5000 (2021).
- ⁶²W. C. Qiulei Wang, Lei Yan, “Drlinfluids,” GitHub. <https://github.com/venturi123/DRLinFluids> (2022).